# Earth's Future

**Key Points:**

- We track cyclones, anticyclones, jets, mesoscale convective systems (MCSs), atmospheric rivers, fronts, and equatorial waves
- Extreme precipitation is typically associated with multiple atmospheric phenomena that interact across scales
- MCSs are involved in most extreme precipitation events in the tropics and many sub-tropical and mid-latitude regions

**Supporting Information:**

Supporting Information may be found in the online version of this article.

**Correspondence to:**

A. F. Prein,
prein@ucar.edu

# The Multi-Scale Interactions of Atmospheric Phenomenon in Mean and Extreme Precipitation

**Andreas F. Prein[1]** , **Priscilla A. Mooney[2]** , and **James M. Done[1]**

[1]National Center for Atmospheric Research, Boulder, CO, USA, [2]NORCE, Bjerknes Centre for Climate Research, Bergen, Norway

**Abstract** Climate change increases the frequency and intensity of extreme precipitation, which in combination with rising population enhances exposure to major floods. An improved understanding of the atmospheric processes that cause extreme precipitation events would help to advance predictions and projections of such events. To date, such analyses have typically been performed rather unsystematically and over limited areas (e.g., the U.S.) which has resulted in contradictory findings. Here we present the Multi-Object Analysis of Atmospheric Phenomenon algorithm that uses a set of 12 common atmospheric variables to identify and track tropical and extra-tropical cyclones, cut-off lows, frontal zones, anticyclones, atmospheric rivers (ARs), jets, mesoscale convective systems (MCSs), and equatorial waves. We apply the algorithm to global historical data between 2001–2020 and associate phenomena with hourly and daily satellite-derived extreme precipitation estimates in major climate regions. We find that MCSs produce the vast majority of extreme precipitation in the tropics and some mid-latitude land regions, while extreme precipitation in mid and high-latitude ocean and coastal regions are dominated by cyclones and ARs. Importantly, most extreme precipitation events are associated with phenomena interacting across scales that intensify precipitation. These interactions are a function of the intensity (i.e., rarity) of extreme events. The presented methodology and results could have wide-ranging applications including training of machine learning methods, Lagrangian-based evaluation of climate models, and process-based understanding of extreme precipitation in a changing climate.

**Plain Language Summary** Increases in intense precipitation and faster onsets of droughts are just two of many precipitation-related extreme events that worsen under progressive climate change. Surprisingly little is known about the weather systems that are driving these changes in many regions around the world. In order to better predict and prepare for these events, scientists need an improved understanding of the causes of the involved atmospheric processes and their interactions. A new algorithm called the Multi-Object Analysis of Atmospheric Phenomenon has been developed to identify and track different types of weather systems, such as tropical and extra-tropical cyclones, that can lead to extreme precipitation. The algorithm was applied to global weather data from 2001 to 2020. The results showed that certain types of weather systems, such as mesoscale convective systems, are frequently involved in causing the most extreme precipitation. Additionally, the study found that most extreme precipitation events are caused by a combination of different weather systems working together and that these interactions differ depending on event intensity. This research could be useful for improving climate models and understanding how extreme precipitation is likely to change in the future.

## 1. Introduction

Many studies have examined the atmospheric drivers of intense precipitation. Kunkel et al. (2012) analyzed the drivers of 1-in-5-year occurrence of daily precipitation events in the U.S. during the period 1908–2009 and found that more than 70% of extreme precipitation in the central U.S. is related to frontal systems and less than 10% to mesoscale convective systems (MCSs). In similar work, Schumacher and Johnson (2006) found a much greater contribution from MCSs of 75% of warm-season intense precipitation events in the eastern U.S. This highlights (a) the difficulty in differentiating the dominant phenomena that cause intense precipitation and (b) that intense events may be influenced by multiple phenomena that interact across spatial scales. This is confirmed by a recent review of intense precipitation events and their large-scale meteorology over North America by Barlow et al. (2019), who concludes that events are often related to mesoscale processes that are triggered, enhanced, or organized by larger-scale processes.

The above examples illustrate that classifying extreme precipitation-producing phenomena is challenging and that scientists might attribute the same event to different phenomena depending on their data analysis methods and scientific focus. Additionally, manually classifying extreme events is labor-intensive, time-consuming, and difficult to reproduce. In contrast, automatic algorithms can be very efficient in classifying atmospheric features and allow analyzing vast data sets much more efficiently than manual classification. Automatic algorithms are frequently used to identify atmospheric phenomena such as tropical cyclones (TC) (Hodges et al., 2017; Ullrich et al., 2021; Vitart et al., 1997), extratropical cyclones (Neu et al., 2013), frontal zones (Berry et al., 2011), atmospheric rivers (ARs) (Guan & Waliser, 2015; Shields et al., 2018), and MCSs (Davis et al., 2009; Feng et al., 2021; A. F. Prein et al., 2020). However, these algorithms can be prone to creating spurious results and their outcomes can be sensitive to the classification settings (A. F. Prein et al., 2020). To date, most feature classification algorithms have been designed to identify single phenomena, which can lead to similar issues as explained in the manual classification above.

Here we present the Multi-Object Analysis of Atmospheric Phenomenon (MOAAP) algorithm that uses a set of 12 common atmospheric variables to track MCSs, surface cyclones, mid-level cyclones, cut-off lows (COLs), Tropical Cyclone (TCs), anticyclones, jets, frontal zones, ARs, equatorial Kelvin waves, Rossby waves (RW), mixed Rossby gravity waves (MRGs), inertia gravity waves (IGWs), and eastward propagating gravity waves. Our goal is to understand the contribution of each phenomenon to mean and extreme precipitation on a close-to-global scale and to highlight interactions of different phenomena in producing extreme precipitation. The paper focuses on the past 20 years because of the availability of global hourly precipitation and cloud observations. A climatological data set of atmospheric phenomena is established that can be used in future model evaluation, climate variability, and climate change assessments. All of the identified phenomena have multiple classification criteria in existing literature, which introduces epistemic uncertainty in our analyses. Where possible, we compare our results with published references and discuss potential sources of differences. We select classification criteria based on previously published literature and, where necessary, develop new criteria that reduce the input data demand while reproducing similar statistics. We acknowledge that there are other potentially important phenomena such as stationary thunderstorms that can cause extreme precipitation events. These are not included in this analysis due to the lack of observational data and our study's objective to minimize input data requirements.

## 2. Data and Methods

A guiding principle of our approach is to use a minimum set of variables to identify and track a maximum number of atmospheric phenomena. We only use standard output variables that are commonly available from reanalyzes and climate models. The following section introduces the selected variables and the methods used for the feature classification.

### 2.1. Data

We use hourly global or almost global data sets to identify and track features within the period from January 2000 to December 2020. In doing so, we combine variables from the fifth generation reanalysis from the European Center for Medium-Range Weather Forecasts (ERA5) (Hersbach et al., 2020), NASA global precipitation measurement (GPM) integrated multi-satellite retrievals for GPM (IMERG) (Huffman, Bolvin, Braithwaite, et al., 2015), and National Oceanic and Atmospheric Administration GPM Merged Infrared (GPM_MERGIR) (Janowiak et al., 2017).

ERA5 is a state-of-the-art reanalysis product that assimilates a large variety of in situ and remote-sensing observations into the global Integrated Forecast System model to create hourly estimates of the state of the atmosphere within the period 1950 to present on a 30 km grid (Hersbach et al., 2020). The following nine variables are used in our analysis: pressure at sea level, zonal and meridional wind speed at 850 and 200 hPa, air temperature at 850 hPa, eastward and northward integrated water vapor flux (IVT), and geopotential height at 500 hPa. We decided to not use ERA5 precipitation and longwave outgoing radiation since we found that these fields largely deviated from observational products likely due to the coarse grid spacing and the need to parameterize deep convection in ERA5 (Rasmussen & et al., 2023). Blending observational fields with reanalysis fields for the identification of phenomena did not result in problems likely due to the assimilation of these data sets into the ERA5 system.

Instead of precipitation from ERA5, we use estimates from IMERG version 6 that are available from 2000 to the present on a global 0.1° grid every 30 min. Data pole-ward of ±60° is only partially available for grid cells without snow on the ground. IMERG merges satellite microwave precipitation estimates with satellite infrared observations and precipitation gauge records. Although IMERG has a fairly high spatiotemporal spacing, its effective resolution is several times coarser than its grid spacing (Guilloteau & Foufoula-Georgiou, 2020). We also acknowledge that gridded precipitation data sets may under-represent the most extreme precipitation recorded by gauges. Nonetheless, Feng et al. (2021) show that using IMERG precipitation to track MCSs over the U.S. leads to similar results compared to using hourly stage-IV (Lin & Mitchell, 2005) radar-based precipitation estimates.

For cloud brightness temperature we use observations from GPM_MERGIR that merge a range of European, Japanese, and U.S. geostationary satellites observations onto a 60°S–60°N 4-km grid every 30-min starting in 2000 (Huffman, Bolvin, Nelkin, & Tan, 2015). There are occasionally areas with missing data, particularly in the South Pacific. Areas with missing data are treated as "not a number" values and no cloud features are identified in these regions. Brightness temperature is typically no standard model output but can be estimated from longwave outgoing radiation at the top of the atmosphere (Wu & Yan, 2011; Yang & Slingo, 2001), which is widely available.

We calculate hourly precipitation accumulations from IMERG and use GPM_MERGIR observations at the full hour to align their temporal resolution with the one from ERA5. Additionally, we regrid these data sets to the ERA5 grid using bi-linear interpolation. All of the analyses presented in this paper are performed on the 30 km regular grid of ERA5 using hourly data.

### 2.2. Methods

#### 2.2.1. Identification and Tracking of Objects

Our tracking algorithm is based on the connectedness (i.e., adjacent in space and time) of objects. It is conceptually similar to the Method for Object-Based Diagnostic Evaluation Time Domain (MTD) (Davis et al., 2009; Clark et al., 2014; A. F. Prein et al., 2020) and a further developed version of the python-based MCS tracker used in Poujol et al. (2020) and A. Prein et al. (2021). Our tracker applies the following five steps.

1. A threshold is applied to the three-dimensional (time, latitude, longitude) variable of interest resulting in a binary field where all grid cells that are above/below the threshold are set to one (these are the objects of interest), and all other cells are set to zero. Larger absolute threshold values generally result in fewer, smaller, and more intense objects. For surface cyclones, this threshold is ≤8 hPa in the surface pressure anomaly field.
2. The binary field is provided to the Python label function of the multidimensional image processing tool (ndimage), which is part of the SciPy package. This function identifies objects that are connected in space and time (horizontally or diagonally) and assigns them with a unique label (i.e., index) resulting in a feature matrix.
3. For long-lived objects we apply a merging and splitting function to the feature matrix. This function merges or breaks up objects that are connected in time but not in space. For example, if two objects merge, the smaller object will end at the previous timestep and will be assimilated into the bigger object. Similarly, when an object splits into two objects the larger of the two objects will continue while the smaller object will be treated as a new feature (see Figure 1 for an example including surface cyclones). The merging and splitting function allows to define a temporal threshold that ensures that only longer-lived merged and split objects are relabeled. For instance, we only relabel a split object if it exists for longer than 4-hr.
4. From the entire population of identified objects a subset is selected that fulfills a range of criteria that are specific to the atmospheric phenomena under consideration (see Table 1 and the following subsection). All objects already fulfill the intensity criteria because of the thresholding performed in step 1. All phenomena except for fronts have temporal criteria that remove short-lived (typically small) objects from the analysis and some phenomena have a minimum area threshold. Additional criteria such as the geometric criteria for ARs or a minimum latitude to detect fronts are also considered.
5. We calculate object characteristics once all objects that qualify as a specific phenomenon are identified.

#### 2.2.2. Object Characteristics

The calculation of object characteristics allows us to perform statistical analyses by for example, pooling objects within a region. Characteristics are calculated by using the object label to mask the object from its background field (e.g., AR objects are used to extract IVT data). From this data, we calculate object characteristics for each
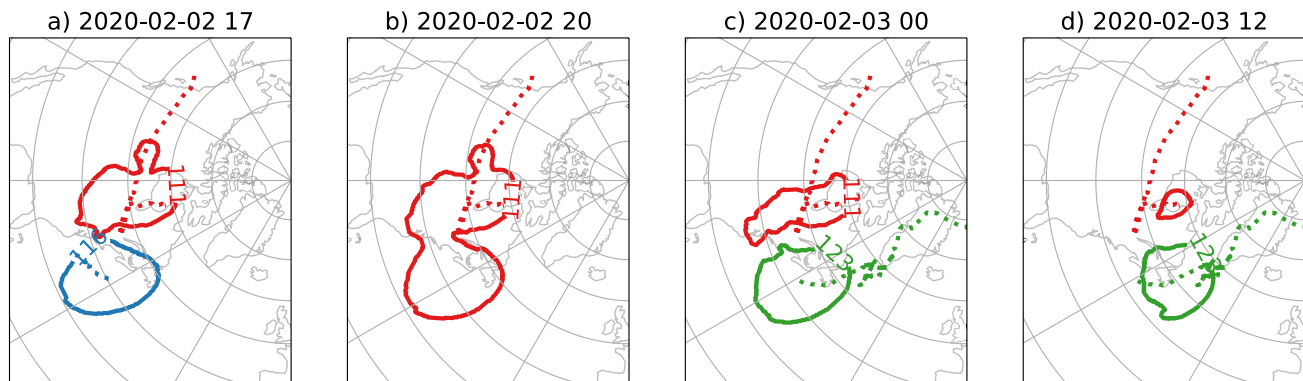
**Figure 1.** Example for merging and tracking of surface cyclones over eastern North America. Cyclone number 111 (red) and 110 (blue) collided on 2 February 2020 (a) resulting in the termination of the smaller cyclone (110, (b)). 6 hr later, cyclone 111 splits into two cyclones resulting in the genesis of a new cyclone (123, (c)). Dotted lines show the track of each cyclone. Cyclone 111 ends over Hudson Bay and cyclone 123 moves over Greenland and enters the Arctic Ocean (d).

time step (i.e., hour). Those characteristics include the area, sum (e.g., accumulated precipitation), minimum, mean, maximum, and center of mass. The latter is used to calculate the object speed given by the displacement of the center of mass between two time steps. The object speed can fluctuate largely over time mainly due to the merging and splitting of objects, which can result in large changes in the center of mass from one time step to the next (see Figure 1). We tested alternative methods to calculate the translation speed of objects such as maximizing the pattern correlation by moving the object from the previous time step spatially over the object of the current time step. While this is computationally much more expensive it does not provide a significant improvement over the center of mass-based method.

### 2.2.3. Cyclone and Anticyclone Detection

Multiple approaches have been proposed to track cyclones (Neu et al., 2013). Some use minimum thresholds in local gradients (Blender & Schubert, 2000), closed contours, and/or minimum pressure (Bardin & Polonsky, 2005). Also, different variables are used to track cyclones, each having benefits and drawbacks (Hodges et al., 2003). The most common variables are sea level pressure (SLP), geopotential height at low levels, and vorticity (Neu et al., 2013). We identify a variety of cyclones including surface cyclones, mid-level cyclones, COLs, and TC. A TC, for instance, will always be detected as a surface low and could also be identified as a mid-level cyclone at the same time, meaning that the same cyclone can be detected as multiple phenomena.

We decided to use SLP for tracking surface cyclones and anticyclones and 500 hPa geopotential height (Z500) for tracking mid-level cyclones. These two variables are widely available as a standard model output. The downside of using SLP is that orographic effects can create artificial gradients that might be identified as phenomena (Simmonds & Murray, 1999) but SLP is beneficial to identify shallow cyclones that have circulations close to the surface. We do not use a closed contour criterion because we want our algorithm to work on regional and global domains. Rather than tracking absolute values of SLP and Z500, we track their anomalies that are derived in three steps. First, we smooth the original field with a uniform square filter with a length of 100 km. This removes small-scale noise and local orographic effects from the SLP and Z500 field. Second, we calculate the background environment in which cyclones exist. For this, we use a uniform square filter with a side length of 3,000 km and a temporal extent of 78 hr. In the third and final step, we calculate SLP and Z500 anomalies by subtracting the background state from the filtered field from step one. Contiguous areas in the anomaly field that are $\leq -8$ hPa for SLP or $-80$ m for Z500 and exist for more than 12 hr are identified as cyclones.

Using the anomaly field for tracking cyclones rather than the absolute SLP/Z500 field has the benefit of being able to track cyclones at lower latitudes that are typically not very deep, but can be very impactful. Figure 2b shows a representative example of a very slow-moving mid-level cyclone that formed in July 2021 over northeast North America and tracked all the way to central Europe causing major flooding in the United Kingdom, western Germany, and neighboring Netherlands, Belgium, and Luxembourg. Note that no surface cyclone was detected in this case.
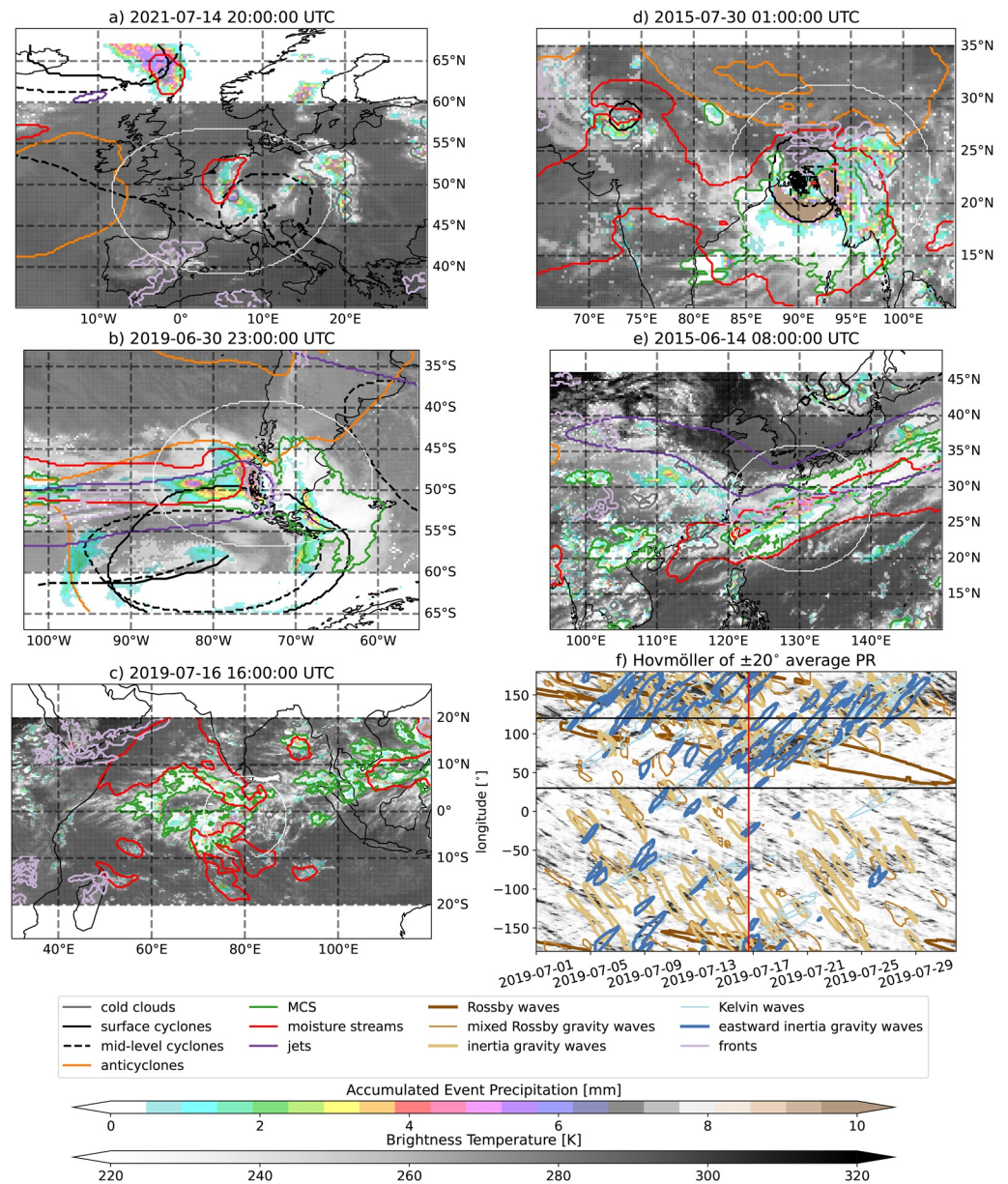
**Figure 2.** Involved features during the Central European floods in 2021 (a), Southern Chile in 2019 (b), heavy tropical precipitation in July 2019 (c), (f), monsoonal extreme precipitation in July 2015 (d), and extreme rainfall embedded in the Meiyu Front in June 2015 (e). Colored-filled contours show hourly GPM-IMERG precipitation and gray contours show GPM_MERGIR brightness temperatures. Contours show integrated vapor transport streams (red), cold cloud tops (gray), surface cyclones (black), 500 hPa cyclones (dashed black), anticyclones (orange), frontal zones (light purple), mesoscale convective systems (green), and jet streams (dark purple). Additionally shown are the track of surface (black solid lines) and 500 hPa cyclones (dashed black line). The white circle in panels (a)–(e) indicated the 1,000 km search radius that is used to associate phenomena to extreme rainfall events. Panel (f) shows a Hovmöller diagram for zonally average precipitation around the equator (±20°; black contours) including the location of equatorial Rossby waves (dark brown), equatorial mixed Rossby gravity waves (medium brown), inertia gravity waves (light brown), Kelvin waves (light blue), and eastward inertia gravity waves (dark blue). The black horizontal lines indicate the region that is shown in (c) and the red vertical line shows the corresponding time.

Anticyclones can also be detected in the SLP anomaly field. We define anticyclones as contiguous areas of SLP anomalies ≥6 hPa that exist for at least 12 hr. The settings for calculating SLP/Z500 anomaly fields and the cyclone and anticyclone anomaly thresholds are based on sensitivity tests and comparisons to existing cyclone tracking studies (not shown).

**Table 1**
*Criteria Used for Feature Classification*

| Feature | Intensity thresholds | Temporal | Spatial/Area | Additional criteria | Breakup |
|---|---|---|---|---|---|
| Surface Cyclones | $P_{anom} \leq -8$ hPa | 12-hr | | | yes |
| Mid-level Cyclones | $Z500_{anom} \leq -80$ m | 12-hr | | | yes |
| COL | must be a mid-level cyclone; must be local minimum; eastward flow pole-ward of cyclone center; front east of cyclone center | | | | yes |
| Tropical Cyclones | $P_{min} \leq 995$ hPa; Tb $\leq 241$ K; warm core T850 $\geq 0°$C; mean T$_{850 hPa} \geq 285$ K | | | max. lat genesis $\leq \pm 35°$; max. lat $\leq \pm 65°$ | no |
| Anticyclones | $P_{anom} \geq 6$ hPa | 12-hr | | | yes |
| IVT Streams | $MS_{min} \geq 0.13$ g/g × m/s | 9-hr | $A_{IVT} \geq 100,000$ km² | | yes |
| Jet | $UV200_{anom} \leq 22$ m s$^{-1}$ | 24-hr | | | yes |
| ARs | IVT $\geq 500$ kg/ms | 9-hr | | min. length $\geq 2,000$ km; length/width $\geq 2$; lat. centroid $\geq \pm 20°$ | yes |
| Mesoscale Convective Systems | max. PR $\geq 3$ mm/hr; Tb $\leq 241$ K; min Tb $\leq 225$ K | 3-hr | $A_{PR \geq 2 mm/h} \geq 2,500$ km²; $A_{Tb \geq 241 K} \geq 40,000$ km² | | no |
| Fronts | | | $A_{FR} \geq 50,000$ km² | lat. $\geq \pm 10°$ | no |
| Kelvin waves | WK-filtered wave amplitude >0.1 | 48-hr | | $\pm 20°$ | yes |
| Rossby waves | WK-filtered wave amplitude >0.05 | 48-hr | | $\pm 20°$ | yes |
| Mixed Rossby-gravity waves | WK-filtered wave amplitude >0.05 | 48-hr | | $\pm 20°$ | yes |
| Eastward inertia gravity waves ($n \leq 0$) | WK-filtered wave amplitude >0.1 | 48-hr | | $\pm 20°$ | yes |
| Inertia gravity waves | WK-filtered wave amplitude >0.2 | 48-hr | | $\pm 20°$ | yes |

*Note*. The following acronyms are used in the table: pressure (P), moisture stream (MS), integrated vapor transport (IVT), brightness temperature (Tb), temperature (T), area (A), 500 hPa geopotential height (Z500), and 200 hPa wind speed (UV200). WK-filtered waves refer to the filtering described in Wheeler and Kiladis (1999).

### 2.2.4. Cut-Off Lows (COLs)

A COL is a cold low-pressure system that occurs in mid-latitudes and sometimes even in subtropical latitudes. COLs occur when polar air is separated from the main belt of low-pressure and cold air. Initially a trough in the upper-air flow, a COL forms a closed circulation extending to the surface. COLs can be flood-producing due to their slow movement speed causing stationary rainfall over a long duration (Hsieh, 1949).

We follow the COL detection algorithm by Muñoz et al. (2020) and assess if mid-level cyclones fulfill all of the following criteria:

- At least 75% of the grid cell in a 350 km ring around the cyclone center (minimum Z500 location) must have 10 m higher Z500 values than the center of the cyclone. The ring thickness is $\pm 2$ grid spacing around the 350 km radius.
- There must be eastward flow in at least one grid point that extends from the center of the COL pole-ward (including grid points within the extent of the mid-level cyclone object). We decided to use wind speed at the 200 hPa for this criterion, which is also used for jet stream detection (see Section 2.2.6), to minimize the number of necessary input variables.
- A frontal zone must exist eastward of the center of the COL. We use fronts as defined in Section 2.2.7.

Muñoz et al. (2020) used an additional fourth criterion that checks for cold cores and a thickness ridge eastward of the low. We neglected this criterion to reduce the number of input variables needed for the analysis.

### 2.2.5. Tropical Cyclone (TCs)

TCs are a sub-set of surface cyclones, we use additional criteria to differentiate TCs from other cyclones. We optimized these criteria based on a comparison to IBTrACS observations (not shown) (Knapp et al., 2010). These criteria are:

- The cyclone minimum SLP must be ≤995 hPa. This ensures that cyclones are sufficiently strong to be considered a TC.
- The TC genesis must be equator-ward of ±35° latitude.
- TC cannot exist pole-ward of ±60° latitude.
- The TC core must be warmer than the average 850 hPa temperature within the cyclone object. This ensures that the TC has a warm core. Optimally, temperatures at higher atmospheric levels should be used to assess the warm core structure of TCs (4–8 km height (Stern & Nolan, 2012)). Using the 850 hPa temperature is a compromise since we use this field for detecting frontal zones and want to minimize the number of necessary algorithm input variables.
- The minimum temperature within the TC at 850 hPa has to be ≥285 K.
- The mean cloud shield brightness temperature (Tb) over the TC object must be ≤241 K. This helps to eliminate cyclones that do not produce deep convection.

### 2.2.6. Jet Streams

Various methods have been used to identify jet streams (Bals-Elsholz et al., 2001; Manney et al., 2011; Strong & Davis, 2006, 2007). Frequently jets are classified by analyzing wind speeds between 400 and 100 hPa for areas that exceed ~30 m s$^{-1}$. We decided to use the same approach as described above for identifying cyclones and rather use wind speed anomalies than absolute wind speeds to identify jets. This has the benefit of being able to identify regions with high winds speeds relative to the background flow but generally seems to lead to similar results. We define jet stream as large-scale features that exceed wind speed anomalies of 22 m s$^{-1}$ at the 200 hPa level over a period of 24 hr. We chose the comparatively lower threshold of 22 m s$^{-1}$ compared to ~30 m s$^{-1}$ since we are analyzing anomaly fields. The requirement of having jet streams last for longer than 24 hr eliminates small-scale objects since the size and duration of objects are positively correlated.

The anomalies are calculated by filtering the 200 hPa wind speed with a 500 km side length uniform filter to remove small-scale variability. Next, the wind background state is calculated by filtering the 200 hPa wind speed with a uniform filter with a side length of 5,000 km over a temporal scale of 78 hr. The anomaly field is the difference between the smoothed field and the background field.

### 2.2.7. Atmospheric Fronts

We use the algorithm proposed by Parfitt et al. (2017) for detecting frontal zones. The frontal variable (F*) is calculated as:

$$F^* = \zeta_p |\nabla(T_p)|, \qquad (1)$$

where $T$ is the air temperature at a pressure surface ($p$; here 850 hPa) and $\zeta_p$ is the curl of the wind vector that is normal to the pressure surface. Next, we calculate the non-dimensional and normalized frontal diagnostic $F$ as:

$$F = \frac{F^*}{f |\nabla T|_0}, \qquad (2)$$

where $f$ is the Coriolis parameter at the corresponding latitude and $|\nabla T|_0 = 0.45$ K/100 km. Fronts are identified in grid cells where $F > 1$. An example of frontal zones is shown in light purple contours in Figure 2e over Southeast Asia (SEA) and the adjacent Pacific. A caveat in using this frontal definition is that grid cells close to the equator can not be analyzed since $f$ becomes zero. Additionally, orographic effects on temperature and wind speed frequently introduce stationary fronts over mountain regions (e.g., see Figure 2b), which complicates the analysis of fronts over areas with steep orographic gradients. We decided to only identify but not track frontal zones since the hourly input data from ERA5 is typically too coarse to connect thin and often fast-moving frontal zones in time.

### 2.2.8. Mesoscale Convective Systems (MCSs)

We track mesoscale ice clouds by masking all grid cells with hourly regridded brightness temperatures with less than or equal to 241 K. We remove all features that do not have cloud shields ≥40,000 km$^2$ for more than 4 hr.

Additionally, MCSs must feature overshooting tops, which are identified as brightness temperatures less than 215 K, peak precipitation intensities of more than 15 mm hr$^{-1}$, and a minimum precipitation area of 5,000 km$^2$ at least once in their lifetime. This or similar thresholds are widely used in identifying MCSs (Feng et al., 2021; Maddox, 1980; A. Prein et al., 2021).

### 2.2.9. Atmospheric Rivers (ARs)

We use IVT to identify AR objects. ARs must have IVT values of at least 500 kg m$^{-1}$ s$^{-1}$ and last at least 9-hr. We decided to use a rather high 500 kg m$^{-1}$ s$^{-1}$ threshold since previous work has shown that it results in more reliable results when applied globally (Reid et al., 2020). All objects that fulfill this criterion are called IVT streams. To classify as an AR, IVT streams must be at least 2,000 km long and must be at least twice as long as wide (Guan & Waliser, 2015; Neiman et al., 2008; Reid et al., 2020; Rutz et al., 2014). Additionally, we demand that the centroid of an AR is poleward of 20°, which helps to eliminate persistent objects in the tropics (e.g., monsoonal circulations) that would otherwise classify as ARs.

### 2.2.10. Equatorial Waves

Equatorial waves are types of atmospheric and oceanic waves that are primarily observed in the tropical regions near the equator (Krishnamurti et al., 2013). These waves are driven by various factors, including the Earth's rotation, interactions between the atmosphere and the ocean, and changes in temperature and pressure. Equatorial waves can be classified into several types based on their characteristics and the mechanisms that drive them. We identify the following equatorial waves:

- Atmospheric Kelvin waves are vertical oscillations of temperature and wind patterns that propagate eastward along the equator, influencing tropical weather and atmospheric circulation and are involved in the Madden-Julian Oscillation (MJO).
- Mixed Rossby-gravity waves occur when RW and gravity waves interact with each other. They are often initiated by convective activity, TC, or topographic features. They exhibit both eastward and westward propagation like RW, but they also possess vertical velocities associated with gravity waves.
- Eastward inertia gravity waves (EIG0) are a combination of inertia waves, or Kelvin waves, and gravity waves. They propagate eastward along the equator, similar to inertia waves, and do not have any meridional nodes. They do not exhibit vertical motion and represent the simplest form of inertia-gravity waves.
- IGWs, in contrast to EIG0, have one or more meridional nodes, meaning there are regions in the wave where the air motion changes from upward to downward or vice versa. This vertical motion is often associated with the vertical displacement of air parcels due to convection.
- Equatorial RW are primarily caused by the conservation of potential vorticity. They move westward in the equatorial regions and are important for tropical (Chatterjee & Goswami, 2004) and global climate patterns for instance through they interact with the MJO (Masunaga et al., 2006). They typically have larger amplitudes and lower frequencies and long wavelengths than IGWs or mixed Rossby-gravity waves (Kiladis et al., 2009) often contribute to heavy rainfall events in the tropics and subtropics through the multi-scale interaction (Fujinami et al., 2014, 2017).

We identify equatorial waves by filtering in the Wheeler-Kiladis wavenumber-frequency domain (Kiladis et al., 2009; Wheeler & Kiladis, 1999; Wheeler et al., 2000). The GPM-IMERG hourly precipitation data ±20° north and south of the equator (Kiladis et al., 2009; Masunaga, 2007) are space-time bandpass filtered at each point, following the method described by Wheeler and Kiladis (1999). Prior to filtering, the data are detrended and tapered using cos20 tapering (Harris, 1978). Subsequently, a 2-dimensional Fast Fourier Transform is applied for filtering. We use a Python implementation of the Wheeler-Kiladis method based on Miyachi (2012) and threshold the wave field to identify wave peaks and track them as objects (see Table 1). Equatorial wave objects must exist for at least 48 hr to be considered in our analyses.

## 3. Results

### 3.1. Case Studies of Interacting Phenomena During Extreme Precipitation Events

We illustrate MOAAP's multi-feature identification approach by showing the atmospheric conditions of five recent extreme precipitation events starting with the central European floods in July 2021 (Figure 2a). The dominant feature is a COL (mid-level cyclone) over central Europe that initiated over northeastern North America,

detached from the general circulation North of Europe, and propagated very slowly over Central Europe. This COL triggered large-scale rainfall with embedded deep convection that caused major flooding. Note that no surface cyclone was detected during this event. Figure 2b shows an AR event in June 2019 that caused major flooding in southern Chile. The AR is co-located with the jet stream, a surface and mid-level cyclone in the South, and an anticyclone in the North. The co-occurrence of pole-ward cyclonic and equator-ward anticyclonic circulation is a common feature in extreme precipitation-producing ARs, as we will show later since this setup is enhancing the eastward moisture flux. A large cluster of MCSs contributed to extreme rainfall in the equatorial Indian Ocean in July 2019 (Figure 2c). This MCS cluster was organized by the interaction of multiple equatorial waves (Figure 2f). Figure 2d shows a stationary monsoonal low-pressure system (surface cyclone) over the northern Bay of Bengal in July 2015 that caused heavy rainfall over a period of multiple days. The cyclone wrapped itself with very moist air visible as a moisture stream object (red contours) and is collocated with an MCS (green contours). The last example shows a heavy precipitation episode caused by the Meiyu/Baiu front in SEA. The front is identified as an elongated object (light purple contours) that is on the northern edge of an AR and south of the Jet stream (purple contours). Multiple MCSs are embedded in the large-scale system.

### 3.2. Scale Analysis of Atmospheric Phenomena

Scale diagrams that visualize the time and spatial scale of various atmospheric phenomena, such as shown in Kotamarthi et al. (2016) (see Figure 7), are useful to understand the spatiotemporal characteristics of motions in the atmosphere. Such diagrams are typically based on expert knowledge. Figure 3 shows a fully data-driven version of a scale diagram based on the tracking results in this study. We can sample meso-alpha to macro-alpha scales (Orlanski, 1975) and hours to weeks since ERA5 has a horizontal grid spacing of ~30 km, hourly output, and we are tracking phenomena 1 month at a time, meaning that phenomena that life from 1 month to the next are split into two. While this increases the frequency of phenomena and reduces their duration, it has little effect on the overall statistics since most phenomena live much shorter than a month. We calculate the length scale of each phenomenon from its area by assuming circular shapes. MCSs have an average lifetime of less than a day and an average length of ~250 km the smallest phenomena that we track while jets are with >1,000 km and ~3 days the largest and longest-lived. Cyclones and anticyclones occupy a wide range of length scales with anticyclones typically being shorter-lived than cyclones. Large cyclones and anticyclones often occur in mid-latitudes while their polar counterparts are typically smaller (not shown). TCs have similar average lifetimes as surface and mid-level cyclones. Equatorial waves, particularly RW, are the longest-lived phenomena that we are tracking and typically last for several days and move the slowest (are shifted toward the top left corner of the diagram). There is a tendency for larger objects to be longer-lived. Generally, these results agree with expectations but the significant amount of overlap between the spatiotemporal space that different phenomena occupy is often misrepresented in existing scale diagrams.

### 3.3. Climatology of Atmospheric Phenomena

Figure 4 shows the climatological frequency of phenomena. These frequencies represent the average number of days that a grid cell is occupied by a phenomenon. Note that this is not the track density but incorporates the phenomenon's spatial extent and duration.

Surface cyclones feature a global hot spot of up to 200 days per year in the Southern Ocean around 60°S and 120°E (Figure 4a). The northern hemisphere features the well-known storm tracks in the North Pacific and North Atlantic. The spatial pattern of cyclone frequencies agrees well with previous studies (Neu et al., 2013; Ullrich & Zarzycki, 2017) but the absolute values are difficult to compare since most studies present track densities instead of phenomenon frequencies. We believe showing the latter is more informative since it better represents the impact of a phenomenon on an area that can extend large distances from its center. Also, monsoon low-pressure systems seem reasonably well captured (Hurley & Boos, 2015). Mid-level cyclone frequencies feature similar spatial patterns to their surface counterparts (Figure 4b) but have a more smooth transition from land to ocean regions (e.g., northeast Atlantic). COLs (Figure 4c) that are a subset of mid-level cyclones have similar frequency patterns but show a secondary maximum over the Iberian Peninsula and the Western Mediterranean in agreement with Muñoz et al. (2020). TCs occur over sub-tropical and mid-latitude ocean regions with a global hotspot in the west Pacific (Figure 4d). Our algorithm erroneously picks up TCs in the South Atlantic, which is similar to Ullrich et al. (2021) and might partly be related to using ERA5 data for TC identification.
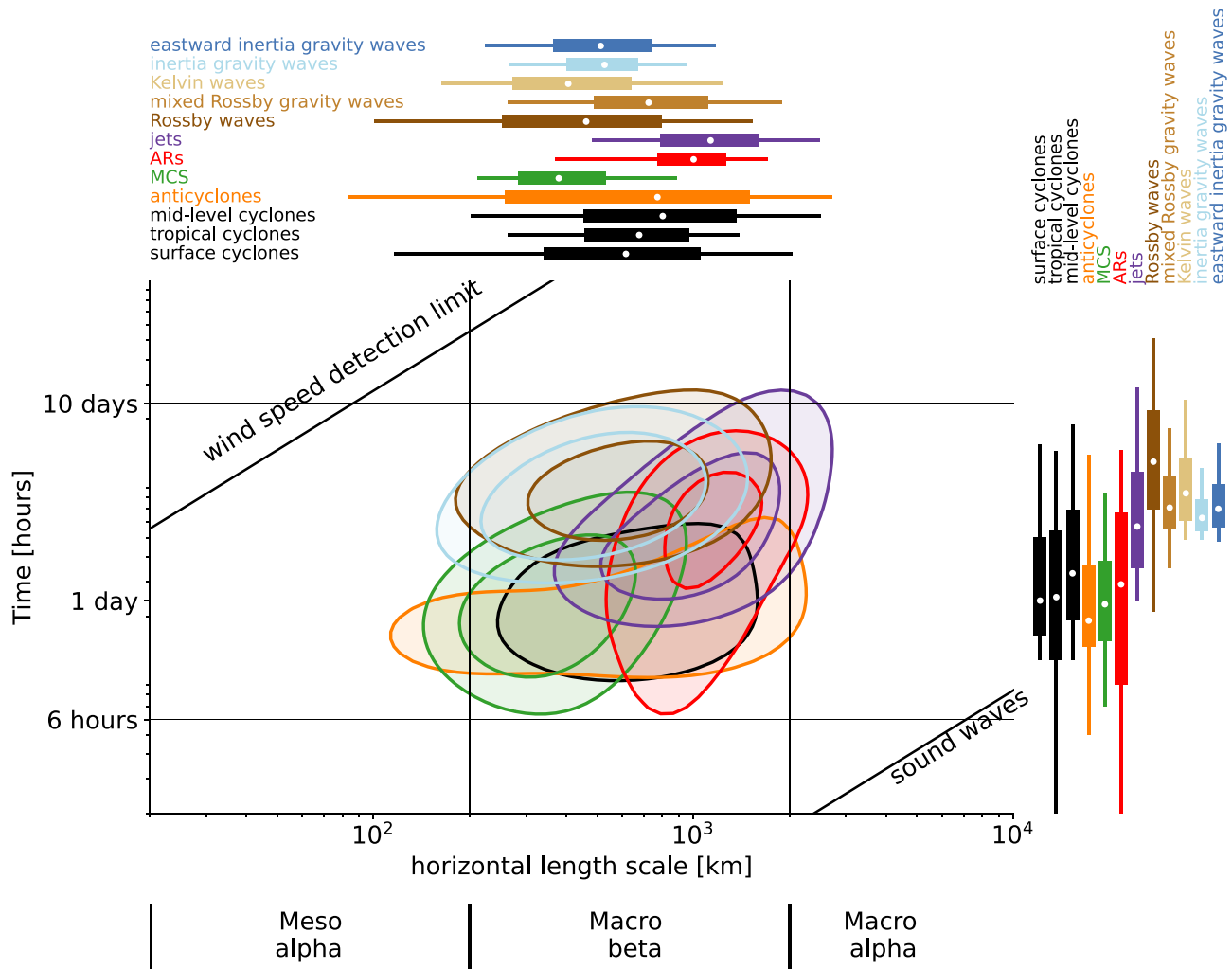
**Figure 3.** Characteristic feature horizontal length scale (*x*-axis) and time scale (*y*-axis) for cyclones (black), anticyclones (orange), mesoscale convective systems (green), atmospheric rivers (red), jets (purple), and westward (brown) and eastward propagating equatorial waves (blue). The contours show 2-dimensional Gaussian kernel density estimates with a bandwidth of 0.4 that was applied to the logarithm of the data. The box-whisker plots show the median (white dot), interquartile range (boxes), 5th to 95th percentile (whiskers), and maximum and minimum (colored circles). Data from 2015 to 2020 is shown. Adding more years does not significantly alter the results.

Anticyclones feature maxima north and south of the area of maximum cyclone frequency in both hemispheres (Figure 4c). There is also a high frequency of anticyclones over Antarctica. In the northern hemisphere, anticyclone frequencies have a local maximum over the eastern Pacific and Atlantic basin and the Beaufort Sea. Further hotspots exist over central Asia, Greenland, and Antarctica that should be interpreted with caution since they are partly a result of interpolating surface pressure to sea level. These frequency patterns agree well with previously published data (Pepler et al., 2019).

Peak jet frequencies occur over SEA and the northwest Pacific with a secondary maximum over the southwest Pacific. Both of these regions have largely zonal oriented jets while the hot spot regions in the Atlantic feature jets that are orientated equator to pole-ward from west to east. These results agree well with previous jet stream climatologies (Koch et al., 2006; Pena-Ortiz et al., 2013).

Our front detection algorithm frequently identifies stationary fronts over regions with steep topography (Figure 2b). Therefore, we decided to mask grid cells that have larger than 25 m average orographic gradients compared to their nine sour-rounding grid cells. Regions with the highest frontal activity are close to the east coasts in northern mid-latitudes. Prominent is the area of the Meiyu/Baiu front in SEA and the northeastern
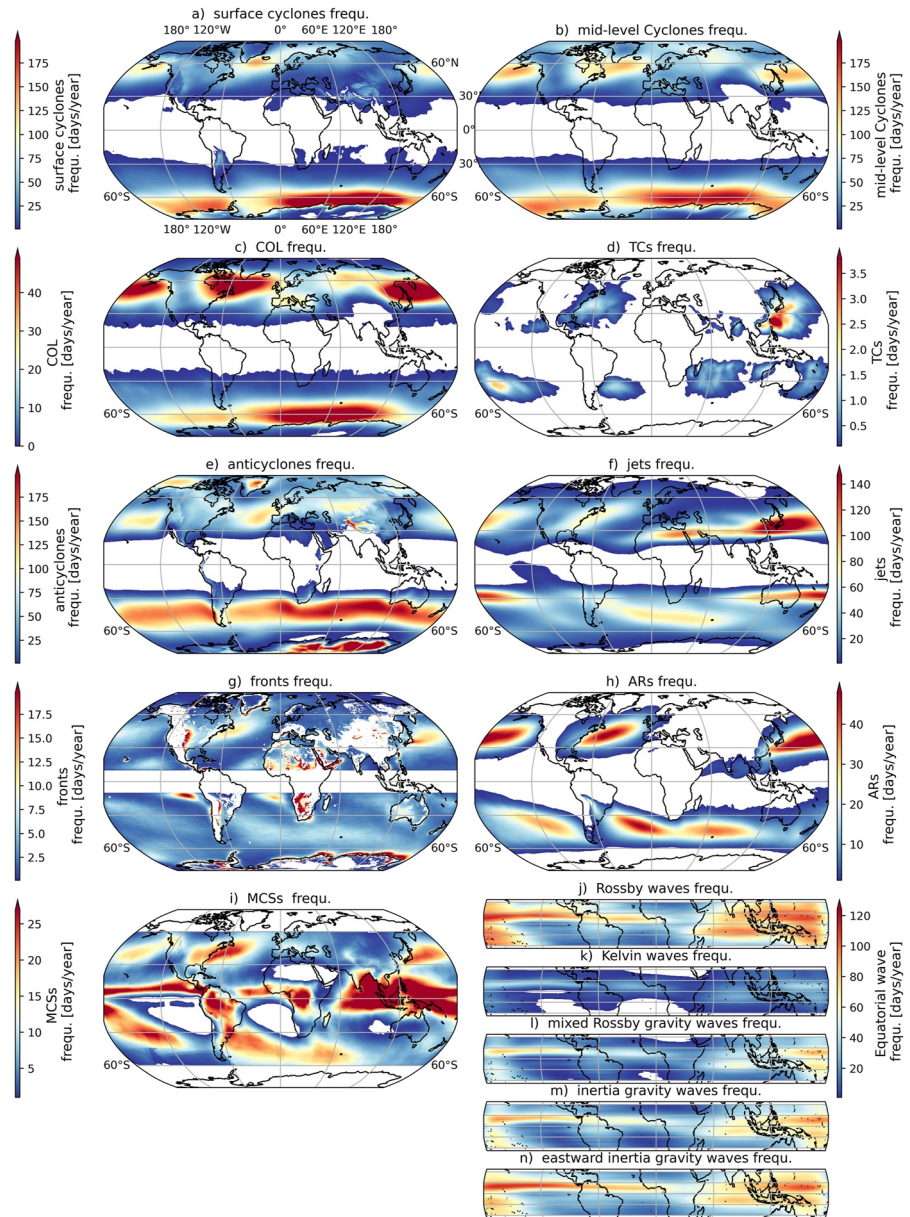
**Figure 4.** Average annual frequency of surface cyclones (a), mid-level cyclones (b), cut-off lows (c), Tropical Cyclone (d), anticyclones (e), jets (f), fronts (g), atmospheric rivers (h), mesoscale convective systems (i), equatorial Rossby waves (j), Kelvin waves (k), mixed Rossby gravity waves (l), inertia gravity waves (IGWs) (m), and eastward inertia gravity waves (n).

Pacific. No prominent hotspots are visible over the southern hemisphere except for subtropical areas west of South America and Africa and coastal regions around Antarctica. Frontal statistics in the latter are likely affected by strong land-ocean and orographic gradients. These general patterns agree well with results shown in Berry et al. (2011) and Parfitt et al. (2017) except for the hotspots in the subtropical southern Pacific and Atlantic.

AR frequencies show maxima over all mid-latitude ocean basins (Figure 4h), and have a characteristic diagonal orientation (equator-ward in the west and pole-ward in the east) that is associated with hot spots in cyclones and anticyclones. ARs occur most frequently between these two hot spot regions, which agrees well with previous research (DeFlorio et al., 2019).

MCSs are most common in the Intertropical Convergence Zone (ITCZ), particularly over the warm pool region, over the Amazon basin, and the Congo basin (Figure 4i). In mid-latitudes, the La Plata basin, the Southeastern
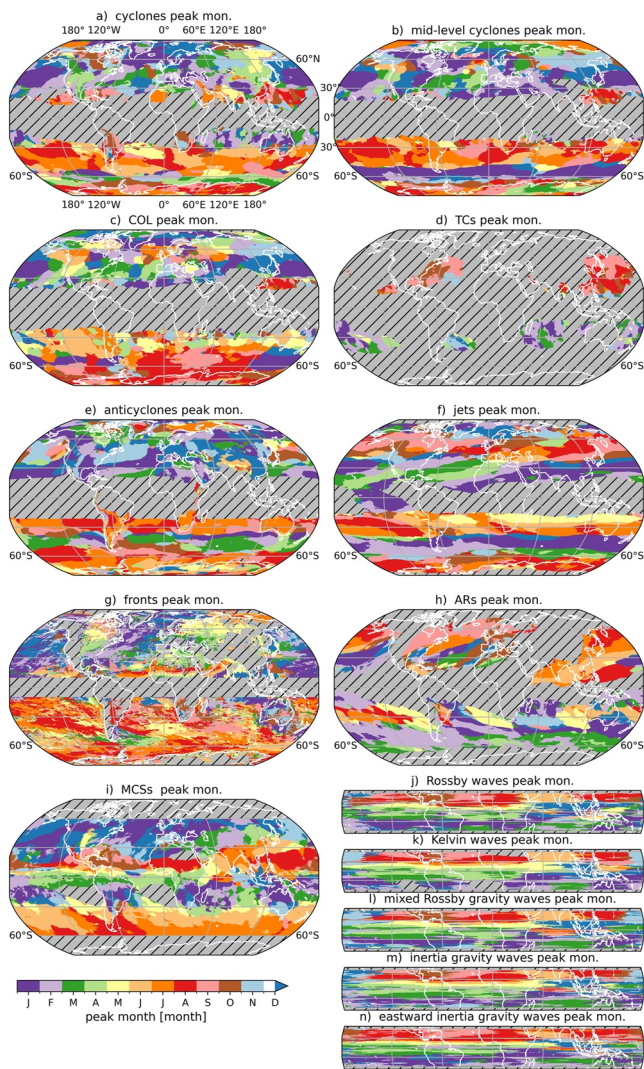
**Figure 5.** Similar to Figure 4 but showing the month with peak feature frequencies. The hatched areas show regions where features are less frequent than once in 4 years.

U.S., and the North Atlantic and North Pacific storm track region feature the highest activities in agreement with Feng et al. (2021).

We track equatorial waves in a latitudinal band of ±20° and find that Kelvin waves are the least frequent while equatorial RW are the most frequent. Generally, equatorial waves are most frequent in the warmpool region and the west Pacific with a band of high frequencies expanding in the northern-eastern equatorial Pacific (Figures 4j–4n).

Figure 5 shows the climatological peak month of phenomena frequencies. It is important to notice that some phenomena have double-peaked annual frequencies, which contributes to some of the spatial variability in Figure 5.

Surface and mid-level cyclones, as well as COL frequencies typically peak in winter meaning during December, January, and February (DJF) in the northern hemisphere and June, July, and August (JJA) in the southern hemisphere (Figure 5a–5c). However, there are some noticeable exceptions such as an April peak of surface cyclones in the western and central U.S. or in northeast Asia. Seasonalities are similar between surface and mid-level cyclones but regional differences exist such as along the U.S. West Coast (mid-level cyclones peak 3 months later) or South Africa (surface cyclones peak in summer while mid-level cyclones peak in winter). The seasonal peak months of TCs are in late summer and early fall in both hemispheres (Figure 5l). An equator-ward migration of anticyclonic activity during JJA is visible in the southern hemisphere (Figure 5e), which is not as obvious in the northern hemisphere. However, jet streams show a pole-ward migration in both hemispheres during summer (Figure 5f). Unsurprisingly, fronts have similar peak months as surface cyclones in most regions although the spatial patterns are more noisy (Figure 5g). ARs reach their peak frequency during January, February, and March (JFM) in most areas of the southern hemisphere while a clear seasonal progression is visible in the north-east Pacific and northeast Atlantic (Figure 5h). Here, northern regions have a late summer peak changing to a winter peak in southern regions. The different mechanisms that cause MCSs are visible in their seasonality (Figure 5i). MCS frequencies in the tropics feature the northward and southward propagation of the ITCZ. Mid-latitude ocean regions frequently feature winter-time maxima while mid-latitude land areas deviate from this pattern and show spring and summer peak frequencies. All equatorial waves have similar peak months and their peak frequencies migrate from south to north between March to August around most of the equator while N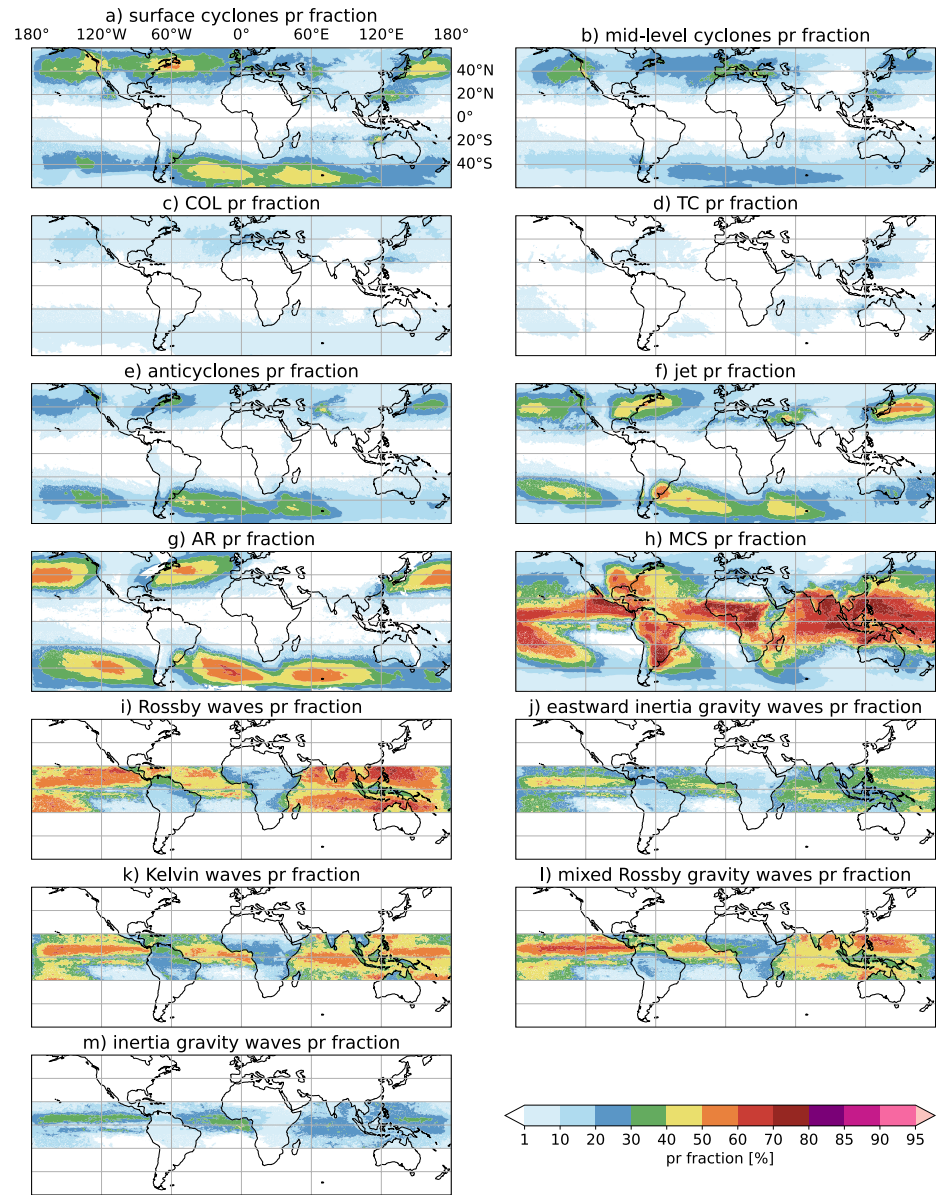ovember to February maxima are partly found over the Maritime Continent likely related to the seasonal maxima of the MJO occurrence at this time (Lu & Hsu, 2017) (Figures 5j–5n).

### 3.4. Phenomena Contribution to Mean and Heavy Precipitation

Here, we discuss the fractional contribution of each phenomenon's precipitation to total annual precipitation (Figure 6) and how frequently each phenomenon contributes to the top 99th percentile hourly precipitation events at each grid cell (Figure 7). The 99th percentile of hourly rainfall is exceeded ~88 times a year. We incorporate the precipitation within each object's extent and the precipitation under mesoscale ice cloud shields that intersect with the phenomenon. For example, for TCs we account for the precipitation in the area of the low-pressure anomaly and the precipitation in the adjacent ice cloud shield (brightness temperatures lower than 241 K).

The Northwest Atlantic is a global hotspot for precipitation from surface cyclones, with more than 50% of annual rainfall associated with surface cyclones (Figure 6a). Total fractions are smaller for mid-level cyclones except for the Mediterranean region and the northeast Pacific (Figure 6b). COLs and TCs (Figures 6c and 6d) have minor contributions to total rainfall and reach regional peak values of 20%–30%. Our estimates of TC contributions to

**Figure 6.** Fraction of precipitation from surface cyclones (a), mid-level cyclones (b), cut-off lows (c), Tropical Cyclone (d), anticyclones (e), jets (f), atmospheric rivers (g), mesoscale convective systems (h), equatorial Rossby waves (i), eastward inertia gravity waves (j), Kelvin waves (k), mixed Rossby gravity waves (l), and inertia gravity waves (m).

total rainfall are smaller than in previous studies—for example, by Rodgers et al. (2001) or Jiang and Zipser (2010) (compare to their Figure 5d). This is because we systematically under-count TC frequencies in areas that Jiang and Zipser (2010) identified as hot spots such as the Northeast and Northwest Pacific (see Figure 8), and second, rather than using a fixed radius around the center of a TC (typically ∼500 km is used), we account for precipitation in the TC object (low-pressure anomaly and precipitation underneath the TC cloud shield. The latter will result in not accounting for TC precipitation in remote cloud bands that are not directly connected to the system.

We commonly do not associate anticyclones with precipitation and this is true for their core regions but precipitation frequently originates across their pole-ward flanks such as shown for the land-falling AR in Figure 2b. This most often happens in the South Atlantic where some regions experience more than 40% of their annual rainfalls in the vicinity of anticyclones (Figure 6a). In the northern hemisphere, the Karakoram region is the hot
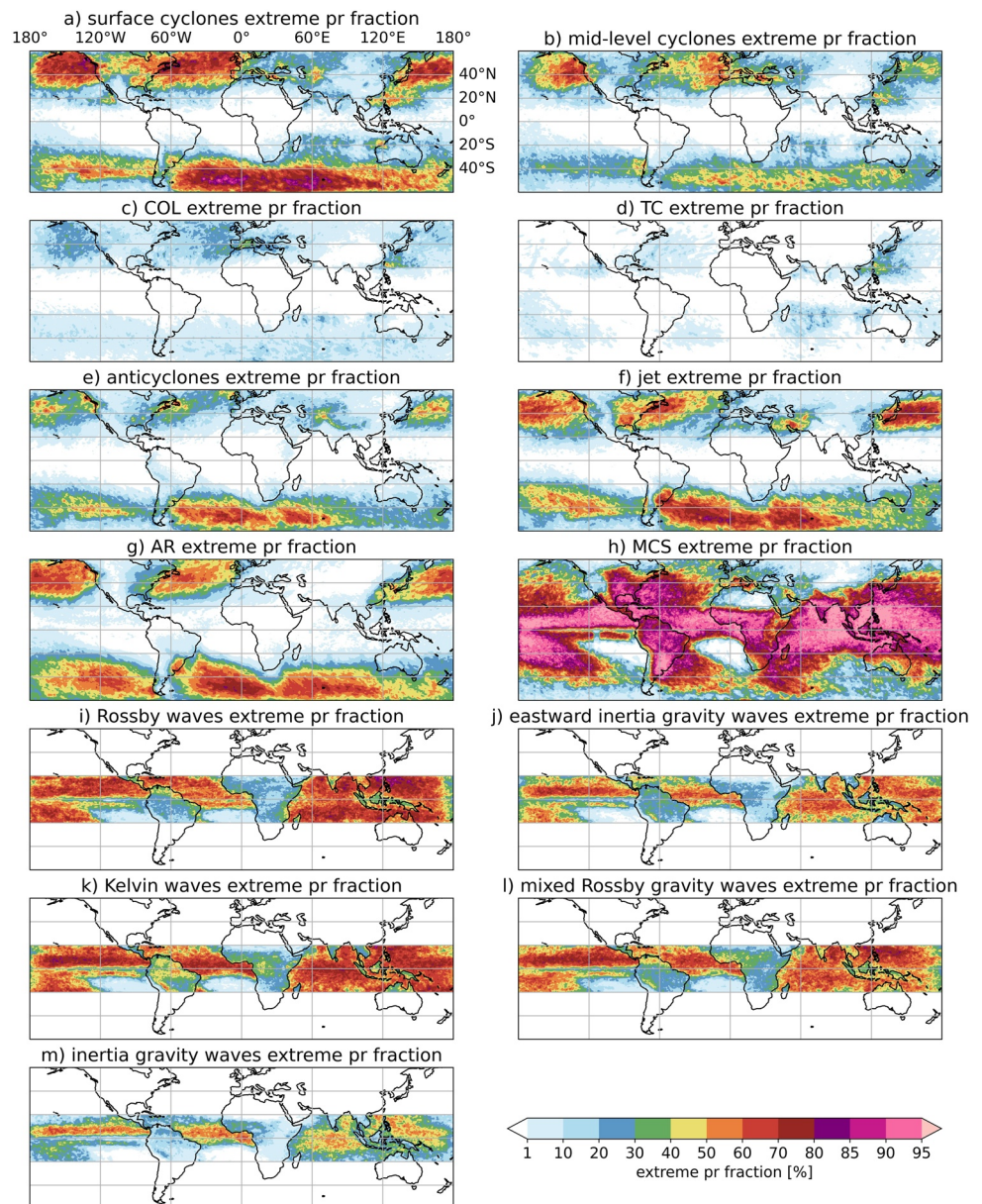
**Figure 7.** Similar as Figure 6 but showing the fraction of events that exceed the hourly 99th percentile precipitation from each phenomenon. We apply a Gaussian spatial filter with a standard deviation of one to reduce small-scale variability.

spot for precipitation under anticyclonic influence, which is related to the frequently detected anticyclones over steep topography partly originating from extrapolating surface pressure from high altitudes to mean sea level.

Jets frequently contribute more than 40% to total precipitation in mid-latitude ocean basins with local maxima exceeding 50% in the Northwest Pacific including Japan and the La Plata basin in South America (Figure 6f). ARs precipitation fractions are also highest in mid-latitude ocean basins with contributions frequently exceeding 50% (Figure 6g). MCSs contribute the majority of precipitation in the tropics and some mid-latitude land regions such as Southeast South America and the Central U.S., which is in good agreement with published literature (Feng et al., 2021; Nesbitt et al., 2006) (Figure 6h). Equatorial Rossby, Kelvin, and MRGs contribute more than 50% to total rainfall over large parts of the tropical oceans while contributions from IGWs are smallest (Figures 6i–6l). It is important to note that we identify equatorial waves by using precipitation meaning that it should not be surprising that they substantially contribute to tropical rainfall. A stark land-sea contrast in precipitation fractions is visible in the entire tropics with lower fractional contributions over land than over ocean regions. This might be
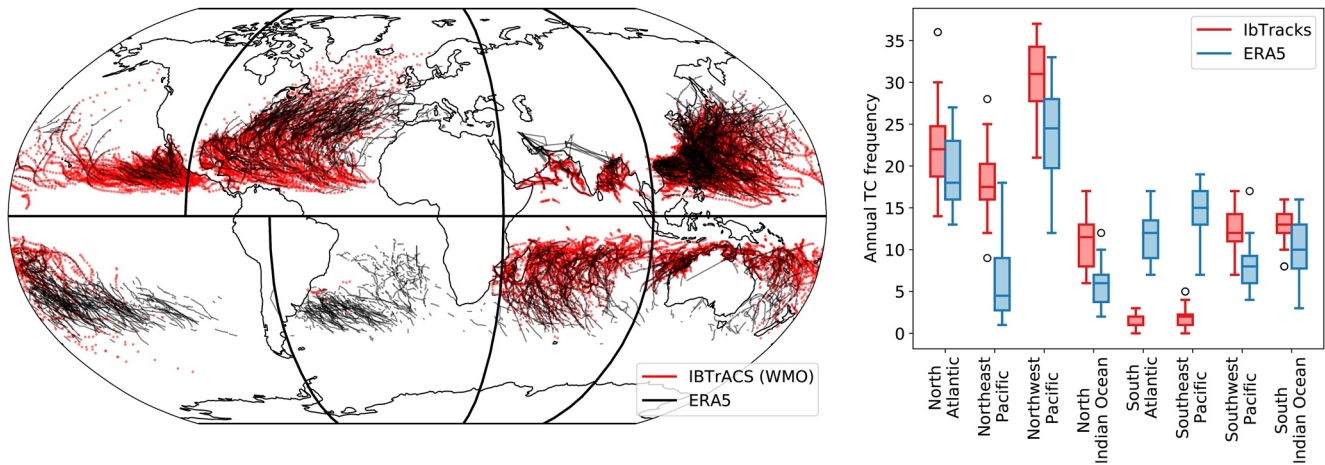
**Figure 8.** Tropical Cyclone (TC) tracks from the IBTrACS World Meteorological Organization (WMO) (red) and our results from tracking TCs in European Center for Medium-Range Weather Forecasts (black) over the period 2001–2020 (left). Only category one or stronger tropical cyclones on the Saffir-Simpson scale are shown. The annual frequency of TCs in each major ocean basin is shown on the right. Box-whisker statistics show the inter-annual variability.

related to the stronger diurnal heating over land causing larger precipitation fractions from local-scale processes compared to ocean regions but more research is needed to understand the exact drivers of the land-sea contrasts.

MCSs dominate heavy hourly precipitation statistics in all regions where they occur (Figure 7h). Contributions exceeding 80% are found in the tropics, subtropics, the eastern U.S., large parts of Sub-Saharan Africa, South America east of the Andes, and China. Equatorial waves are important contributors to heavy hourly rainfall in the tropical ocean regions with the highest contributions from equatorial Rossby, Kelvin and MRGs (Figures 7i–7l). Equatorial waves are known to contribute to extreme precipitation events in the Asian monsoon region (Fujinami et al., 2014, 2017; Kikuchi, 2021; Wang et al., 2006). High fractions of heavy hourly precipitation are related to surface cyclones, jets, and ARS in mid-latitudes (Figures 7a, 7b, 7f, and 7g). Our results agree well with previous analyses and highlight similar hot spot regions of extreme precipitation contributions from ARs (Waliser & Guan, 2017). Heavy precipitation contributions from COLs (Figure 7c) and TCs (Figure 7d) have both peaks of more than 40% in the Northwest Pacific. The overall low contribution of COL and TCs to heavy hourly rainfall is predominantly due to their rarity and their relative contribution to extremes is higher when investigating rarer (more intense) extreme precipitation events as we will show later. Anticyclones play an important role in heavy rainfall production in mid-latitude ocean basins, particularly in the South Atlantic and parts of the South Indian Ocean but also in northern hemispheric coastal regions including the northwest and northeast of North America and the British Isles (Figure 7e). This is in line with recent research that found clear relationships between heatwaves—typically caused by anticyclonic circulation—and hourly rainfall extremes at gauges in mid-latitude regions (Sauter, Fowler, et al., 2023; Sauter, White, et al., 2023).

### 3.5. Phenomena Related to Extreme Precipitation Events

Next, we investigate what phenomena are present in a 1,000 km radius around the top 100 heaviest hourly precipitation events in each IPCC AR6 region (Iturbide et al., 2020). Each event has to be at least 3 days apart to reduce the effect of dependent events in our analysis. Three days are chosen based on an autocorrelation analysis of precipitating events in each sub-region. Note that this method results in selecting much rarer events compared to using the 99th percentile of hourly rainfall in each grid cell used in the previous section. The 1,000 km radius is shown as white circles in Figure 2.

Figure 9 shows that interactions between phenomena during extreme hourly precipitation events are the norm and not the exception in most regions. For instance, the Eastern North America (ENA) region gets all of its top 100 hourly extreme rainfall events from MCSs, 70% of them are near a front, ~60% are influenced by the jet, ~50% are in the vicinity of a surface cyclone (~10% of them are TCs), 40% are close to a mid-level cyclone (~30% of them are COL), and ~40% are near an anticyclone or AR. Most tropical regions get the majority of their extreme hourly precipitation events from MCSs that are often embedded in equatorial waves, while cyclones
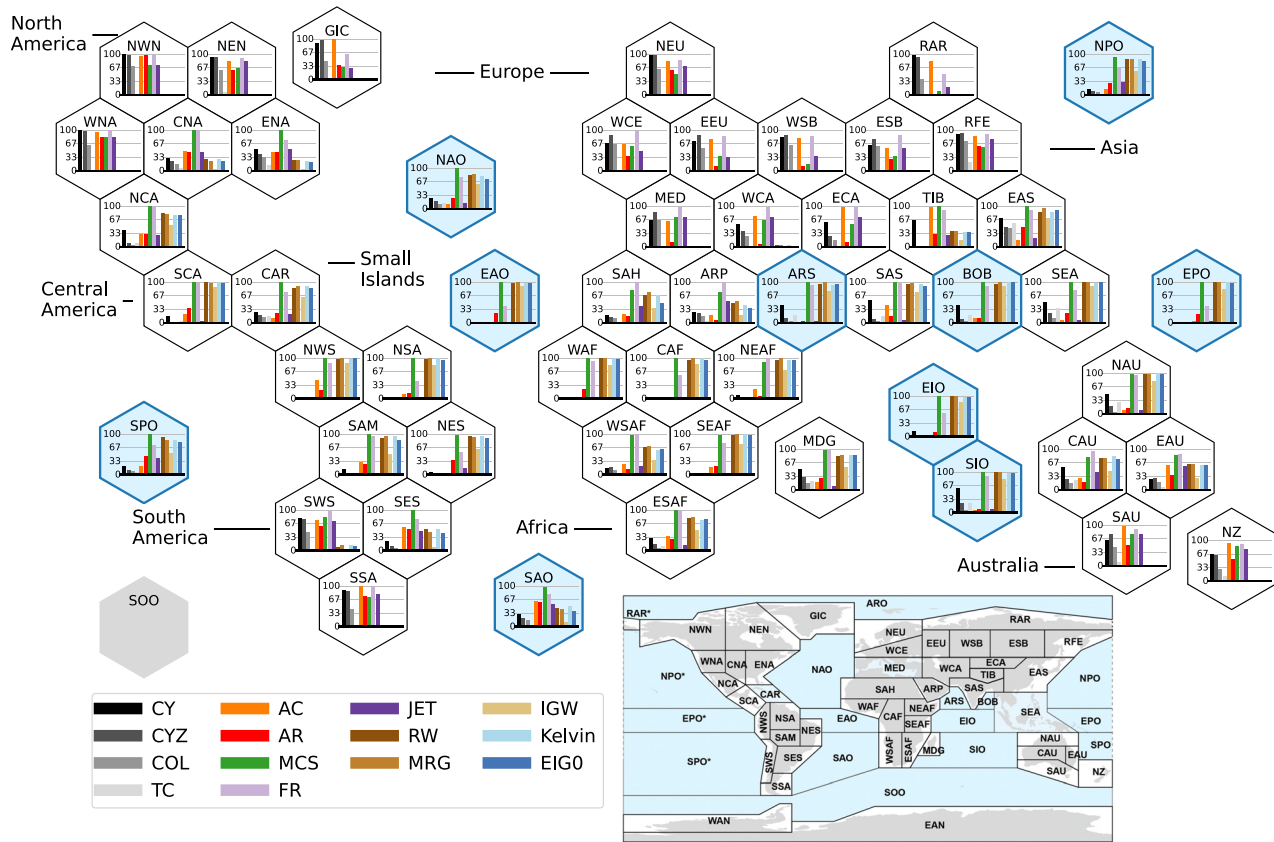
**Figure 9.** Frequency of features in the vicinity (1,000 km radius) of extreme precipitation events in IPCC AR6 regions. We consider the 100 most extreme hourly precipitation events in each region based on GPM-IMERG precipitation. Blue hexagons indicate ocean regions and gray hexagons do not contain GPM-IMERG precipitation data. The location of each region is shown in the map-inlet in the lower right corner (from Iturbide et al. (2020)). Shown are surface cyclones (CYs), mid-level cyclones (CYZs), cut-off lows, tropical cyclones (TCs), anticyclones (ACs), atmospheric rivers (ARs), mesoscale convective systems, fronts (FRs), jets (JETs), equatorial Rossby waves, Kelvin waves (Kelvin), mixed Rossby gravity waves, inertia gravity waves (IGWs), and eastward inertia gravity waves (EIG0).

become dominant in higher latitudes. ARs are major contributors to hourly extreme precipitation events on the west coast of North America (WNA and NWN region; Waliser and Guan (2017)) northern Europe (NEU; Lavers and Villarini (2013)), southern South America (SSA; Viale et al. (2018)), New Zealand (NZ; Reid et al. (2021)), and the south Atlantic Ocean. Noteworthy is the frequent presence of anticyclones in the vicinity of extreme precipitation in mid and high latitudes, which is in line with Sauter, Fowler, et al. (2023). We find similar results when considering the top 100 daily extreme precipitation events (see Figure S1 in Supporting Information S1). The most noteworthy difference is the larger contribution of cyclones in producing mid-latitude daily precipitation extremes. For instance, surface cyclones are associated with hourly precipitation extremes ~40% of the time while this ratio is more than 90% for daily extremes in the ENA region. These differences are likely caused by the increasing importance of rainfall duration for daily extreme events compared to hourly extremes. Slow-moving cyclones can support the production of heavy rainfall over long periods of time.

The contribution of atmospheric phenomena to extreme precipitation is a function of the rarity of extreme events. Figure 10 shows the relative contribution of each phenomenon to extreme hourly precipitation as a function of event intensity (e.g., the 10th event includes the top 10 most intense precipitation events). For instance, in South Eastern South America surface and mid-level cyclones (many of them are COLs) become increasingly important with event intensity/rarity while the co-location of jet streams becomes less important. In Northern Australia, SEA, and ENA TCs are gaining in importance with increasing event rarity. Figure S2 in Supporting Information S1 shows the same statistics for daily precipitation extremes. While differences depend on the region, there is a tendency for stronger cyclonic influence during the rarest daily extreme events compared to hourly events in many regions.
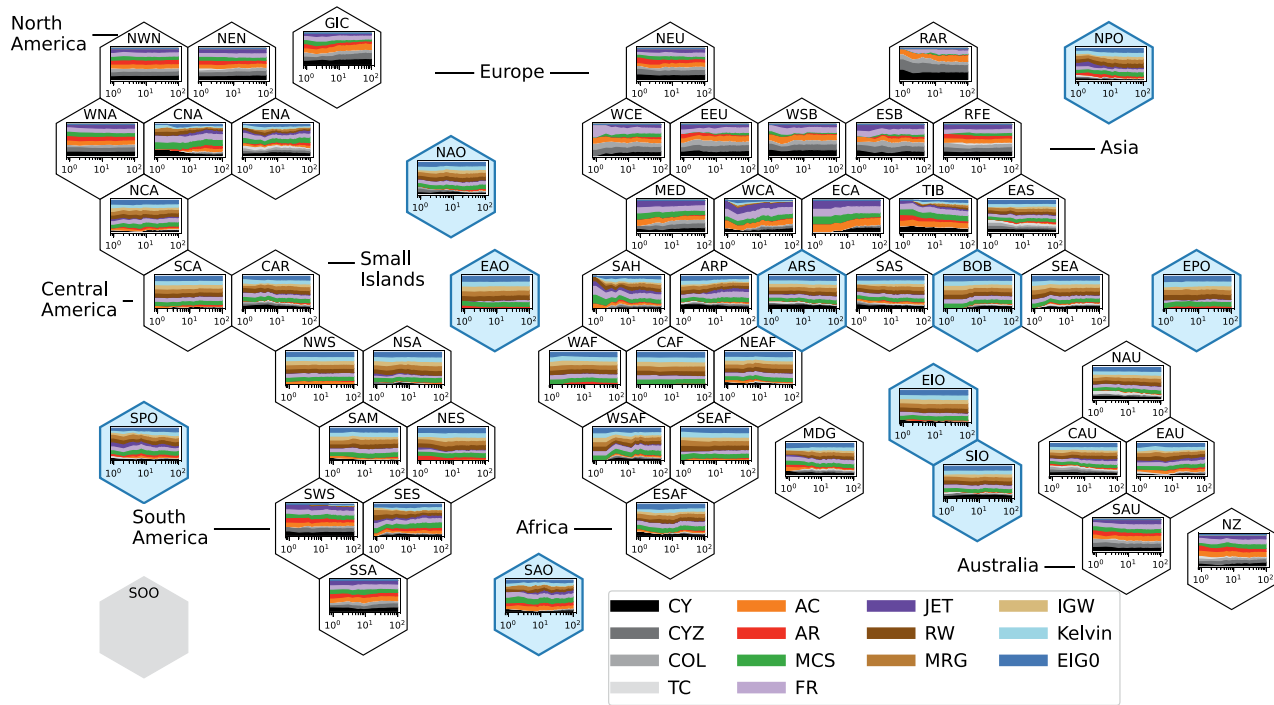
**Figure 10.** As Figure 9 but showing the percent contribution (vertical axis) of atmospheric features dependent on the intensity of the extreme precipitation events with the rarest event on the left and all of the 100 most extreme precipitation events on the right.

To better understand which phenomena combinations are interacting during extreme precipitation events we show the frequency of phenomena co-occurrences in Figure 11. The more colors there are in each panel the more phenomena interactions exist. There are two dominant patterns emerging. Interactions between phenomena in the top half of the triangle that are predominant in the extratropics (jets, fronts, MCSs, ARs, anticyclones, COLs, surface-, and mid-level cyclones; TC interactions are typically infrequent) and interactions of phenomena in the right half of the triangle that are predominant in the tropics (MCSs, fronts, and equatorial waves; jet interactions are infrequent here). Interactions between equatorial waves and cyclones, which appear in the lower-left corner of the triangles, are happening infrequently. Extreme precipitation events that are purely caused by a single phenomenon (top cells in each row) are very rare partly because some of the investigated phenomena are physically connected (e.g., fronts in cyclones). In the tropics, interactions of MCSs with equatorial waves are very common, which is not surprising since MCSs can be triggered by and can amplify equatorial waves (Mathon et al., 2002; Zuluaga & Houze, 2013). In mid-latitudes AR-related extreme precipitation events are frequently co-occurring with a pair of CY and anticyclones as visible in the example in Figure 2b. Generally, the combined occurrence of CY and anticyclones is a common feature in many mid-latitude regions during extreme events. Results for daily extreme events are similar (Figure S3 in Supporting Information S1) with the most noticeable differences in mid-latitudes where interactions with cyclones increase in importance, and in northern high-latitudes where phenomena interactions decrease. Cyclone and anticyclone couples are more common in hourly extreme precipitation events in northwestern North America and NEU compared to daily extreme events.

## 4. Summary and Discussion

In this study, we present the MOAAP algorithm that identifies and tracks surface-, mid-level, and TC, COLs, anticyclones, ARs, jets, MCSs, frontal zones, and four types of equatorial waves. We apply MOAAP to data from 2001 to 2020 to better understand how these features are related to mean and extreme precipitation on a global scale. The main advantage of using a multi-feature-based approach compared to single-feature-based methods that are most common in the existing literature is that it allows us to study interactions between phenomena in extreme precipitation-producing environments. Such interactions are known to be important (Barlow et al., 2019) but are understudied.
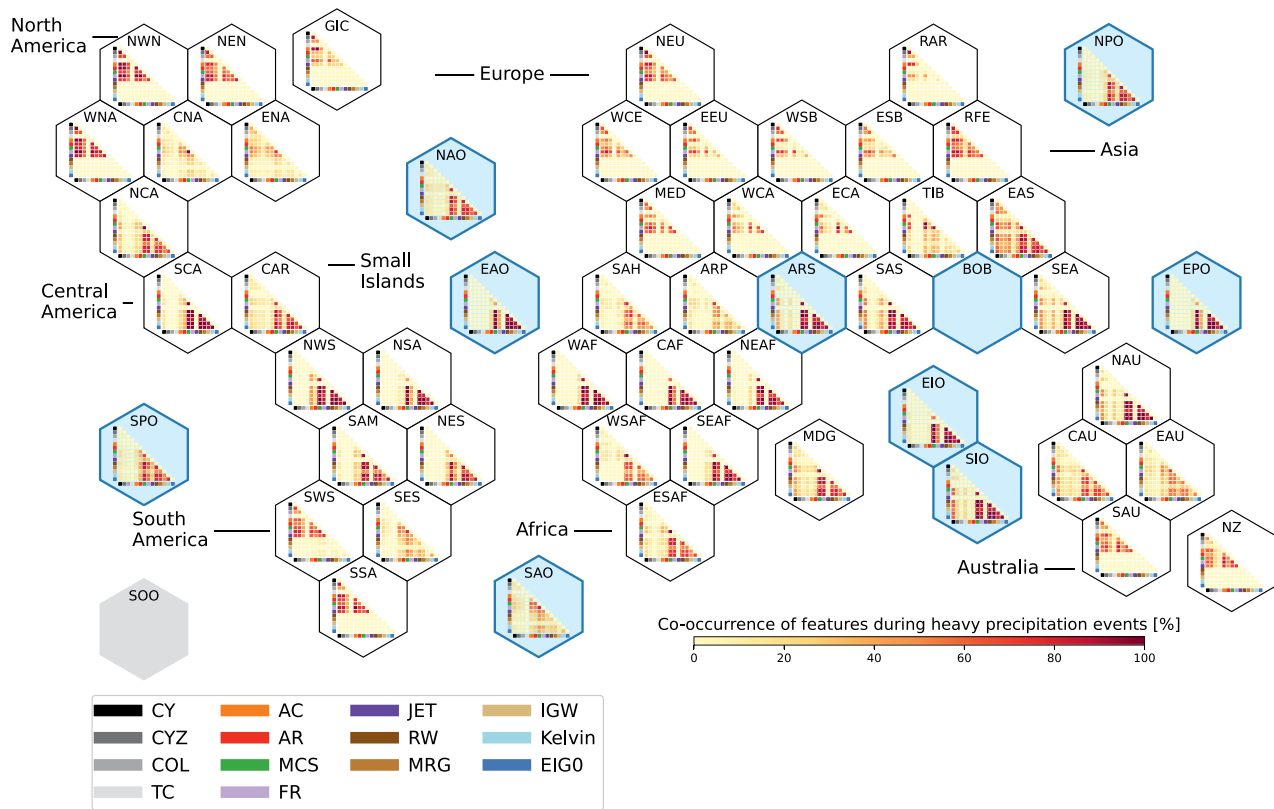
**Figure 11.** Showing the same data as in Figure 9 but highlighting the co-occurrence of features during extreme precipitation events. The colors in the heatmaps show the percent of the time at which features co-occurred. The colors next to the x- and y-axis show the feature as indicated in the legend.

Many approaches exist in the published literature to identify and track individual phenomena such as TC, cyclones, or ARs. Where available, we established methods to maximize the quality of the phenomenon classification by simultaneously minimizing the amount of needed input data. We only use variables that are widely available standard model outputs. The main results and conclusions from this study are:

- Extreme hourly and daily precipitation events are typically caused by multiple atmospheric phenomena that interact on different scales and maximize local precipitation rates. This is intuitive since the need for the alignment and interaction of multiple phenomena is the prime reason why those events are rare and agrees with previous studies over North America (Barlow et al., 2019) and the Himalayas. Therefore, associating extreme precipitation events to a single atmospheric process can be misleading and often oversimplifies the multi-scale interactions involved. It is also important to note that the investigated phenomena are not physically or statistically independent of each other (e.g., cyclones typically have frontal zones).

- MCSs dominate the water cycle in the tropics and continental areas of the sub-tropics such as the Eastern U.S., Southeast South America, and parts of Southern Africa in agreement with previous findings (Feng et al., 2021; Nesbitt et al., 2006). Hourly and daily precipitation extremes are almost exclusively related to MCSs in these regions.

- TCs are a minor contributor to the global water cycle and are of secondary importance for extreme hourly and daily precipitation production. However, this is mainly due to how we define extremes in our analyses and TCs might play a much more significant role in extreme statistics when higher-end extremes and longer time periods would be considered (e.g., the one-in-a-hundred-year event). The advent of high-resolution climate modeling (Haarsma et al., 2016) and particularly km-scale climate modeling (Mahoney et al., 2021; A. F. Prein et al., 2015; Stevens et al., 2019) could help to alleviate some of the observational record-length issues that limit our understanding of high-impact extreme events.

- At higher latitudes, pairs of cyclones and anticyclones play an important role in extreme precipitation production. The co-occurrence of these two phenomena increases moisture convergence and transport. This is a

prime mechanism in regions with strong AR events but also plays an important role in other regions such as in central and Northeastern Asia.

- Interactions between equatorial waves and MCSs are the prime extreme precipitation-producing mechanism in the tropics. However, equatorial waves are less important for extreme events over land than over the ocean indicating that more local scale effects such as sea breezes, orographic effects, or land-atmosphere coupling play an important role.

The findings listed above should be interpreted alongside the following caveats related to our approach.

- The frontal detection algorithm often identifies fronts over steep topography and coastlines. This leads to an overestimation of precipitation related to fronts in these regions. Additionally, hourly model output is typically not sufficient to track frontal objects and only allows us to study them as 2D features.
- The TC tracking algorithm could be improved, particularly in the South Atlantic and South Pacific basins. Identifying warm cores at higher tropospheric levels would be beneficial but would increase the input data volume.
- The thresholds to identify phenomena (see Table 1) could be scale dependent and might have to be re-tuned particularly when applied to much coarser resolution data (i.e., one degree or larger). The thresholds can be easily changed in the MOAAP algorithm to optimize it to various input data sets.
- IMERG precipitation does not cover high latitudes. Although data is provided on a 0.1° grid the effective resolution of IMERG precipitation can be up to 100 km (Guilloteau & Foufoula-Georgiou, 2020) meaning that hourly rainfall rates (particularly extremes) are smoothed. This can result in erroneous detection of extreme hourly rainfall events compared to station data and might bias our analysis toward phenomena that create large precipitation footprints (e.g., cyclones, MCSs) compared to for example, smaller thunderstorms, that are not well captured. Additionally, IMERG has known deficiencies over mountain regions (Bartsotas et al., 2018; Huffman, 2019).

Future work will focus on addressing these caveats. Additionally, MOAAP will be applied as a lagrangian evaluation tool to global and regional climate model simulations and to improve our understanding of climate change impacts on the occurrence of phenomena, phenomena characteristics, and their relation to mean and extreme precipitation. Future work might also focus on adding additional low-frequency phenomena to MOAAP such as the MJO, Boreal Summer Intraseasonal Oscillation (Kikuchi, 2021) in the tropics, and quasi-stationary RW (Coumou et al., 2014) in the mid-latitudes, which have been shown to correspond to extreme wet and hot events. Additionally, identifying smaller-scale convection and phenomena in the land surface or ocean could provide further insights into the physical processes contributing to extreme precipitation, particularly concerning interactions in the coupled earth system. Finally, the results from this feature-based analysis could be used to train machine learning algorithms, most of which currently rely on labeling features by hand (Kashinath et al., 2021).

## Data Availability Statement

ERA-5 reanalysis data can be accessed from the Copernicus Climate Data Store (Copernicus, 2023). The GPM_ MERGIR brightness temperature observations can be downloaded from the NASA server (GPM-MERGIR, 2023) and GPM-IMERG precipitation data can also be accessed from NASA (GPM-IMERG, 2023). The MOAAP code can be downloaded from GitHub (Prein, 2023a). The multi-phenomenon data set that was created and analyzed in this study can be accessed through (Prein, 2023b). An online tutorial that allows users to run the MOAAP algorithm interactively can be accessed here (Prein, 2023c).

## References

Bals-Elsholz, T. M., Atallah, E. H., Bosart, L. F., Wasula, T. A., Cempa, M. J., & Lupo, A. R. (2001). The wintertime Southern Hemisphere split jet: Structure, variability, and evolution. *Journal of Climate*, *14*(21), 4191–4215. https://doi.org/10.1175/1520-0442(2001)014<4191:twshsj>2.0.co;2

Bardin, M. Y., & Polonsky, A. (2005). North Atlantic oscillation and synoptic variability in the European-Atlantic region in winter. *Izvestiya - Atmospheric and Oceanic Physics*, *41*(2), 127–136.

Barlow, M., Gutowski, W. J., Gyakum, J. R., Katz, R. W., Lim, Y.-K., Schumacher, R. S., et al. (2019). North American extreme precipitation events and related large-scale meteorological patterns: A review of statistical methods, dynamics, modeling, and trends. *Climate Dynamics*, *53*(11), 6835–6875. https://doi.org/10.1007/s00382-019-04958-z

Bartsotas, N., Anagnostou, E., Nikolopoulos, E., & Kallos, G. (2018). Investigating satellite precipitation uncertainty over complex terrain. *Journal of Geophysical Research: Atmospheres*, *123*(10), 5346–5359. https://doi.org/10.1029/2017jd027559

Berry, G., Reeder, M. J., & Jakob, C. (2011). A global climatology of atmospheric fronts. *Geophysical Research Letters*, *38*(4), L04809. https://doi.org/10.1029/2010gl046451

Blender, R., & Schubert, M. (2000). Cyclone tracking in different spatial and temporal resolutions. *Monthly Weather Review*, *128*(2), 377–384. https://doi.org/10.1175/1520-0493(2000)128<0377:ctidsa>2.0.co;2

Chatterjee, P., & Goswami, B. N. (2004). Structure, Genesis and scale selection of the tropical quasi-biweekly mode. *Quarterly Journal of the Royal Meteorological Society*, *130*(599), 1171–1194. https://doi.org/10.1256/qj.03.133

Clark, A. J., Bullock, R. G., Jensen, T. L., Xue, M., & Kong, F. (2014). Application of object-based time-domain diagnostics for tracking precipitation systems in convection-allowing models. *Weather and Forecasting*, *29*(3), 517–542. https://doi.org/10.1175/waf-d-13-00098.1

Copernicus (2023). ERA5 hourly data on single levels from 1979 to present [Dataset]. Copernicus Climate Change Service (C3S) Climate Data Store (CDS). https://doi.org/10.24381/cds.adbb2d47

Coumou, D., Petoukhov, V., Rahmstorf, S., Petri, S., & Schellnhuber, H. J. (2014). Quasi-resonant circulation regimes and hemispheric synchronization of extreme weather in boreal summer. *Proceedings of the National Academy of Sciences of the United States of America*, *111*(34), 12331–12336. https://doi.org/10.1073/pnas.1412797111

Davis, C. A., Brown, B. G., Bullock, R., & Halley-Gotway, J. (2009). The method for object-based diagnostic evaluation (MODE) applied to numerical forecasts from the 2005 NSSL/SPC Spring Program. *Weather and Forecasting*, *24*(5), 1252–1267. https://doi.org/10.1175/2009waf2222241.1

DeFlorio, M. J., Waliser, D. E., Guan, B., Ralph, F. M., & Vitart, F. (2019). Global evaluation of atmospheric river subseasonal prediction skill. *Climate Dynamics*, *52*(5–6), 3039–3060. https://doi.org/10.1007/s00382-018-4309-x

Feng, Z., Leung, L. R., Liu, N., Wang, J., Houze, R. A., Jr., Li, J., et al. (2021). A global high-resolution mesoscale convective system database using satellite-derived cloud tops, surface precipitation, and tracking. *Journal of Geophysical Research: Atmospheres*, *126*(8), e2020JD034202. https://doi.org/10.1029/2020jd034202

Fujinami, H., Sato, T., Kanamori, H., & Murata, F. (2017). Contrasting features of monsoon precipitation around the Meghalaya Plateau under westerly and easterly regimes. *Journal of Geophysical Research: Atmospheres*, *122*(18), 9591–9610. https://doi.org/10.1002/2016jd026116

Fujinami, H., Yasunari, T., & Morimoto, A. (2014). Dynamics of distinct intraseasonal oscillation in summer monsoon rainfall over the Meghalaya–Bangladesh–western Myanmar region: Covariability between the tropics and mid-latitudes. *Climate Dynamics*, *43*(7–8), 2147–2166. https://doi.org/10.1007/s00382-013-2040-1

GPM-IMERG. (2023). GPM-IMERG half-hourly precipitation retrieval [Dataset]. Retrieved from https://gpm.nasa.gov/data/imerg

GPM-MERGIR. (2023). GPM-IMERG half-hourly brightness temperature observations. [Dataset]. Retrieved from https://disc.gsfc.nasa.gov/datasets/GPM_MERGIR_1/summary

Guan, B., & Waliser, D. E. (2015). Detection of atmospheric rivers: Evaluation and application of an algorithm for global studies. *Journal of Geophysical Research: Atmospheres*, *120*(24), 12514–12535. https://doi.org/10.1002/2015jd024257

Guilloteau, C., & Foufoula-Georgiou, E. (2020). Multiscale evaluation of satellite precipitation products: Effective resolution of IMERG. In *Satellite precipitation measurement* (pp. 533–558). Springer.

Haarsma, R. J., Roberts, M. J., Vidale, P. L., Senior, C. A., Bellucci, A., Bao, Q., et al. (2016). High resolution model intercomparison project (HighResMIP v1. 0) for CMIP6. *Geoscientific Model Development*, *9*(11), 4185–4208. https://doi.org/10.5194/gmd-9-4185-2016

Harris, F. J. (1978). On the use of windows for harmonic analysis with the discrete Fourier transform. *Proceedings of the IEEE*, *66*(1), 51–83. https://doi.org/10.1109/proc.1978.10837

Hersbach, H., Bell, B., Berrisford, P., Hirahara, S., Horányi, A., Muñoz-Sabater, J., et al. (2020). The ERA5 global reanalysis. *Quarterly Journal of the Royal Meteorological Society*, *146*(730), 1999–2049. https://doi.org/10.1002/qj.3803

Hodges, K., Cobb, A., & Vidale, P. L. (2017). How well are tropical cyclones represented in reanalysis datasets? *Journal of Climate*, *30*(14), 5243–5264. https://doi.org/10.1175/jcli-d-16-0557.1

Hodges, K. I., Hoskins, B. J., Boyle, J., & Thorncroft, C. (2003). A comparison of recent reanalysis datasets using objective feature tracking: Storm tracks and tropical easterly waves. *Monthly Weather Review*, *131*(9), 2012–2037. https://doi.org/10.1175/1520-0493(2003)131<2012:acorrd>2.0.co;2

Hsieh, Y.-P. (1949). An investigation of a selected cold vortex over North America. *Journal of the Atmospheric Sciences*, *6*(6), 401–410. https://doi.org/10.1175/1520-0469(1949)006<0401:aioasc>2.0.co;2

Huffman, G. (2019). IMERG V06 quality index. Retrieved from https://gpm.nasa.gov/sites/default/files/2020-02/IMERGV06_QI_0.pdf

Huffman, G. J., Bolvin, D. T., Braithwaite, D., Hsu, K., Joyce, R., Xie, P., & Yoo, S.-H. (2015). NASA global precipitation measurement (GPM) integrated multi-satellite retrievals for GPM (IMERG). *Algorithm Theoretical Basis Document (ATBD) Version*, *4*, 26.

Huffman, G. J., Bolvin, D. T., Nelkin, E. J., & Tan, J. (2015). Integrated multi-satellitE retrievals for GPM (IMERG) technical documentation. *Nasa/Gsfc Code*, *612*(47), 2019.

Hurley, J. V., & Boos, W. R. (2015). A global climatology of monsoon low-pressure systems. *Quarterly Journal of the Royal Meteorological Society*, *141*(689), 1049–1064. https://doi.org/10.1002/qj.2447

Iturbide, M., Gutiérrez, J. M., Alves, L. M., Bedia, J., Cerezo-Mota, R., Cimadevilla, E., et al. (2020). An update of IPCC climate reference regions for subcontinental analysis of climate model data: Definition and aggregated datasets. *Earth System Science Data*, *12*(4), 2959–2970. https://doi.org/10.5194/essd-12-2959-2020

Janowiak, J., Joyce, B., & Xie, P. (2017). Merged IR V1. In A. Savtchenko & M. D. Greenbelt (Eds.), *Goddard Earth sciences data and information services center (GES DISC)*. https://doi.org/10.5067/P4HZB9N27EKU

Jiang, H., & Zipser, E. J. (2010). Contribution of tropical cyclones to the global precipitation from eight seasons of TRMM data: Regional, seasonal, and interannual variations. *Journal of Climate*, *23*(6), 1526–1543. https://doi.org/10.1175/2009jcli3303.1

Kashinath, K., Mudigonda, M., Kim, S., Kapp-Schwoerer, L., Graubner, A., Karaismailoglu, E., et al. (2021). ClimateNet: An expert-labeled open dataset and deep learning architecture for enabling high-precision analyses of extreme weather. *Geoscientific Model Development*, *14*(1), 107–124. https://doi.org/10.5194/gmd-14-107-2021

Kikuchi, K. (2021). The boreal summer intraseasonal oscillation (BSISO): A review. *Journal of the Meteorological Society of Japan Series II*, *99*(4), 933–972. https://doi.org/10.2151/jmsj.2021-045

Kiladis, G. N., Wheeler, M. C., Haertel, P. T., Straub, K. H., & Roundy, P. E. (2009). Convectively coupled equatorial waves. *Reviews of Geophysics*, *47*(2), RG2003. https://doi.org/10.1029/2008rg000266

Knapp, K. R., Kruk, M. C., Levinson, D. H., Diamond, H. J., & Neumann, C. J. (2010). The international best track archive for climate stewardship (IBTrACS) unifying tropical cyclone data. *Bulletin of the American Meteorological Society*, *91*(3), 363–376. https://doi.org/10.1175/2009bams2755.1

Koch, P., Wernli, H., & Davies, H. C. (2006). An event-based jet-stream climatology and typology. *International Journal of Climatology: A Journal of the Royal Meteorological Society*, *26*(3), 283–301. https://doi.org/10.1002/joc.1255

Kotamarthi, R., Mearns, L., Hayhoe, K., Castro, C. L., & Wuebbles, D. (2016). *Use of climate information for decision-making and impacts research: State of our understanding*. (Tech. Rep.). Argonne National Laboratory Argonne United States.

Krishnamurti, T., Stefanova, L., Misra, V., Krishnamurti, T., Stefanova, L., & Misra, V. (2013). Tropical waves and tropical depressions. *Tropical Meteorology: An Introduction*, 121–141.

Kunkel, K. E., Easterling, D. R., Kristovich, D. A., Gleason, B., Stoecker, L., & Smith, R. (2012). Meteorological causes of the secular variations in observed extreme precipitation events for the conterminous United States. *Journal of Hydrometeorology*, *13*(3), 1131–1141. https://doi.org/10.1175/jhm-d-11-0108.1

Lavers, D. A., & Villarini, G. (2013). The nexus between atmospheric rivers and extreme precipitation across Europe. *Geophysical Research Letters*, *40*(12), 3259–3264. https://doi.org/10.1002/grl.50636

Lin, Y., & Mitchell, K. E. (2005). 1.2 the NCEP stage II/IV hourly precipitation analyses: Development and applications. In *Proceedings of the 19th conference hydrology* (Vol. 10). American Meteorological Society.

Lu, W., & Hsu, P.-C. (2017). Factors controlling the seasonality of the Madden-Julian oscillation. *Dynamics of Atmospheres and Oceans*, *78*, 106–120. https://doi.org/10.1016/j.dynatmoce.2017.04.002

Maddox, R. A. (1980). Mesoscale convective complexes. *Bulletin of the American Meteorological Society*, *61*(11), 1374–1387. https://doi.org/10.1175/1520-0477(1980)061<1374:mcc>2.0.co;2

Mahoney, K., McColl, C., Hultstrand, D. M., Kappel, W. D., McCormick, B., & Compo, G. P. (2021). Blasts from the past: Reimagining historical storms with model simulations to modernize dam safety and flood risk assessment. *Bulletin of the American Meteorological Society*, 1–35.

Manney, G., Hegglin, M. I., Daffer, W., Santee, M., Ray, E., Pawson, S., et al. (2011). Jet characterization in the upper troposphere/lower stratosphere (UTLS): Applications to climatology and transport studies. *Atmospheric Chemistry and Physics*, *11*(12), 6115–6137. https://doi.org/10.5194/acp-11-6115-2011

Masunaga, H. (2007). Seasonality and regionality of the Madden–Julian oscillation, Kelvin wave, and equatorial Rossby wave. *Journal of the Atmospheric Sciences*, *64*(12), 4400–4416. https://doi.org/10.1175/2007jas2179.1

Masunaga, H., L'Ecuyer, T. S., & Kummerow, C. D. (2006). The Madden–Julian oscillation recorded in early observations from the tropical rainfall measuring mission (TRMM). *Journal of the Atmospheric Sciences*, *63*(11), 2777–2794. https://doi.org/10.1175/jas3783.1

Mathon, V., Laurent, H., & Lebel, T. (2002). Mesoscale convective system rainfall in the Sahel. *Journal of Applied Meteorology and Climatology*, *41*(11), 1081–1092. https://doi.org/10.1175/1520-0450(2002)041<1081:mcsrit>2.0.co;2

Miyachi, T. (2012). *kf_filter.py*. GitHub. Retrieved from https://github.com/tmiyachi/mcclimate/blob/master/kf_filter.py

Muñoz, C., Schultz, D., & Vaughan, G. (2020). A midlatitude climatology and interannual variability of 200-and 500-hPa cut-off lows. *Journal of Climate*, *33*(6), 2201–2222. https://doi.org/10.1175/jcli-d-19-0497.1

Neiman, P. J., Ralph, F. M., Wick, G. A., Lundquist, J. D., & Dettinger, M. D. (2008). Meteorological characteristics and overland precipitation impacts of atmospheric rivers affecting the West Coast of North America based on eight years of SSM/I satellite observations. *Journal of Hydrometeorology*, *9*(1), 22–47. https://doi.org/10.1175/2007jhm855.1

Nesbitt, S. W., Cifelli, R., & Rutledge, S. A. (2006). Storm morphology and rainfall characteristics of TRMM precipitation features. *Monthly Weather Review*, *134*(10), 2702–2721. https://doi.org/10.1175/mwr3200.1

Neu, U., Akperov, M. G., Bellenbaum, N., Benestad, R., Blender, R., Caballero, R., et al. (2013). IMILAST: A community effort to intercompare extratropical cyclone detection and tracking algorithms. *Bulletin of the American Meteorological Society*, *94*(4), 529–547. https://doi.org/10.1175/bams-d-11-00154.1

Orlanski, I. (1975). A rational subdivision of scales for atmospheric processes. *Bulletin of the American Meteorological Society*, 527–530.

Parfitt, R., Czaja, A., & Seo, H. (2017). A simple diagnostic for the detection of atmospheric fronts. *Geophysical Research Letters*, *44*(9), 4351–4358. https://doi.org/10.1002/2017gl073662

Pena-Ortiz, C., Gallego, D., Ribera, P., Ordonez, P., & Alvarez-Castro, M. D. C. (2013). Observed trends in the global jet stream characteristics during the second half of the 20th century. *Journal of Geophysical Research: Atmospheres*, *118*(7), 2702–2713. https://doi.org/10.1002/jgrd.50305

Pepler, A., Dowdy, A., & Hope, P. (2019). A global climatology of surface anticyclones, their variability, associated drivers and long-term trends. *Climate Dynamics*, *52*(9), 5397–5412. https://doi.org/10.1007/s00382-018-4451-5

Poujol, B., Prein, A. F., & Newman, A. J. (2020). Kilometer-scale modeling projects a tripling of Alaskan convective storms in future climate. *Climate Dynamics*, *55*(11), 3543–3564. https://doi.org/10.1007/s00382-020-05466-1

Prein, A. F. (2023a). Multi object analysis of atmospheric phenomenon (MOAAP) [Software]. Zenodo. https://doi.org/10.5281/zenodo.7561616

Prein, A., Rasmussen, R., Wang, D., & Giangrande, S. (2021). Sensitivity of organized convective storms to model grid spacing in current and future climates. *Philosophical Transactions of the Royal Society A*, *379*(2195), 20190546. https://doi.org/10.1098/rsta.2019.0546

Prein, A. F. (2023b). Atmospheric features based on remote sensing and ERA5 observations from 2001-2020 [Dataset]. Retrieved from https://app.globus.org/file-manager?origin\_id=55272495-04a8-4486-a07f-eb21ca21797c&origin\_path=\%2F

Prein, A. F. (2023c). MOAAP tutorial [Software]. Retrieved from https://colab.research.google.com/drive/1sD2EsaH34M-rZo1U3w988X46tXBV3OCy?usp=sharing

Prein, A. F., Langhans, W., Fosser, G., Ferrone, A., Ban, N., Goergen, K., et al. (2015). A review on regional convection-permitting climate modeling: Demonstrations, prospects, and challenges. *Reviews of Geophysics*, *53*(2), 323–361. https://doi.org/10.1002/2014rg000475

Prein, A. F., Liu, C., Ikeda, K., Bullock, R., Rasmussen, R. M., Holland, G. J., & Clark, M. (2020). Simulating North American mesoscale convective systems with a convection-permitting climate model. *Climate Dynamics*, *55*(1), 95–110. https://doi.org/10.1007/s00382-017-3993-2

Rasmussen, R. M., Chen, F., Liu, C. H., Ikeda, K., Prein, A. F., Kim, J., et al. (2023). The NCAR-USGS 4-km long-term regional hydroclimate reanalysis over the CONUS. *BAMS*, *104*, E1382–E1408. https://doi.org/10.1175/BAMS-D-21-0326.1

Reid, K. J., King, A. D., Lane, T. P., & Short, E. (2020). The sensitivity of atmospheric river identification to integrated water vapor transport threshold, resolution, and regridding method. *Journal of Geophysical Research: Atmospheres*, *125*(20), e2020JD032897. https://doi.org/10.1029/2020jd032897

Reid, K. J., Rosier, S. M., Harrington, L. J., King, A. D., & Lane, T. P. (2021). Extreme rainfall in New Zealand and its association with atmospheric rivers. *Environmental Research Letters*, *16*(4), 044012. https://doi.org/10.1088/1748-9326/abeae0

Rodgers, E. B., Adler, R. F., & Pierce, H. F. (2001). Contribution of tropical cyclones to the North Atlantic climatological rainfall as observed from satellites. *Journal of Applied Meteorology*, *40*(11), 1785–1800. https://doi.org/10.1175/1520-0450(2001)040<1785:cotctt>2.0.co;2

Rutz, J. J., Steenburgh, W. J., & Ralph, F. M. (2014). Climatological characteristics of atmospheric rivers and their inland penetration over the western United States. *Monthly Weather Review*, *142*(2), 905–921. https://doi.org/10.1175/mwr-d-13-00168.1

Sauter, C., Fowler, H. J., Westra, S., Ali, H., Peleg, N., & White, C. J. (2023). Compound extreme hourly rainfall preconditioned by heatwaves most likely in the mid-latitudes. *Weather and Climate Extremes*, *40*, 100563. https://doi.org/10.1016/j.wace.2023.100563

Sauter, C., White, C. J., Fowler, H. J., & Westra, S. (2023). Temporally compounding heatwave–heavy rainfall events in Australia. *International Journal of Climatology*, *43*(2), 1050–1061. https://doi.org/10.1002/joc.7872

Schumacher, R. S., & Johnson, R. H. (2006). Characteristics of US extreme rain events during 1999–2003. *Weather and Forecasting*, *21*(1), 69–85. https://doi.org/10.1175/waf900.1

Shields, C. A., Rutz, J. J., Leung, L.-Y., Ralph, F. M., Wehner, M., Kawzenuk, B., et al. (2018). Atmospheric river tracking method intercomparison project (ARTMIP): Project goals and experimental design. *Geoscientific Model Development*, *11*(6), 2455–2474. https://doi.org/10.5194/gmd-11-2455-2018

Simmonds, I., & Murray, R. J. (1999). Southern extratropical cyclone behavior in ECMWF analyses during the FROST special observing periods. *Weather and Forecasting*, *14*(6), 878–891. https://doi.org/10.1175/1520-0434(1999)014<0878:secbie>2.0.co;2

Stern, D. P., & Nolan, D. S. (2012). On the height of the warm core in tropical cyclones. *Journal of the Atmospheric Sciences*, *69*(5), 1657–1680. https://doi.org/10.1175/jas-d-11-010.1

Stevens, B., Satoh, M., Auger, L., Biercamp, J., Bretherton, C. S., Chen, X., et al. (2019). DYAMOND: The DYnamics of the atmospheric general circulation modeled on non-hydrostatic domains. *Progress in Earth and Planetary Science*, *6*(1), 1–17. https://doi.org/10.1186/s40645-019-0304-z

Strong, C., & Davis, R. E. (2006). Variability in the altitude of fast upper tropospheric winds over the Northern Hemisphere during winter. *Journal of Geophysical Research*, *111*(D10), D10106. https://doi.org/10.1029/2005jd006497

Strong, C., & Davis, R. E. (2007). Winter jet stream trends over the Northern Hemisphere. *Quarterly Journal of the Royal Meteorological Society: A Journal of the Atmospheric Sciences, Applied Meteorology and Physical Oceanography*, *133*(629), 2109–2115. https://doi.org/10.1002/qj.171

Ullrich, P. A., & Zarzycki, C. M. (2017). TempestExtremes: A framework for scale-insensitive pointwise feature tracking on unstructured grids. *Geoscientific Model Development*, *10*(3), 1069–1090. https://doi.org/10.5194/gmd-10-1069-2017

Ullrich, P. A., Zarzycki, C. M., McClenny, E. E., Pinheiro, M. C., Stansfield, A. M., & Reed, K. A. (2021). TempestExtremes v2. 1: A community framework for feature detection, tracking, and analysis in large datasets. *Geoscientific Model Development*, *14*(8), 5023–5048. https://doi.org/10.5194/gmd-14-5023-2021

Viale, M., Valenzuela, R., Garreaud, R. D., & Ralph, F. M. (2018). Impacts of atmospheric rivers on precipitation in southern South America. *Journal of Hydrometeorology*, *19*(10), 1671–1687. https://doi.org/10.1175/jhm-d-18-0006.1

Vitart, F., Anderson, J., & Stern, W. (1997). Simulation of interannual variability of tropical storm frequency in an ensemble of GCM integrations. *Journal of Climate*, *10*(4), 745–760. https://doi.org/10.1175/1520-0442(1997)010<0745:soivot>2.0.co;2

Waliser, D., & Guan, B. (2017). Extreme winds and precipitation during landfall of atmospheric rivers. *Nature Geoscience*, *10*(3), 179–183. https://doi.org/10.1038/ngeo2894

Wang, B., Webster, P., Kikuchi, K., Yasunari, T., & Qi, Y. (2006). Boreal summer quasi-monthly oscillation in the global tropics. *Climate Dynamics*, *27*(7–8), 661–675. https://doi.org/10.1007/s00382-006-0163-3

Wheeler, M., & Kiladis, G. N. (1999). Convectively coupled equatorial waves: Analysis of clouds and temperature in the wavenumber–frequency domain. *Journal of the Atmospheric Sciences*, *56*(3), 374–399. https://doi.org/10.1175/1520-0469(1999)056<0374:ccewao>2.0.co;2

Wheeler, M., Kiladis, G. N., & Webster, P. J. (2000). Large-scale dynamical fields associated with convectively coupled equatorial waves. *Journal of the Atmospheric Sciences*, *57*(5), 613–640. https://doi.org/10.1175/1520-0469(2000)057<0613:lsdfaw>2.0.co;2

Wu, X., & Yan, J. (2011). Estimating the outgoing longwave radiation from the FY-3B satellite visible infrared radiometer Channel 5 radiance observations. *Chinese Science Bulletin*, *56*(32), 3480–3485. https://doi.org/10.1007/s11434-011-4686-6

Yang, G.-Y., & Slingo, J. (2001). The diurnal cycle in the tropics. *Monthly Weather Review*, *129*(4), 784–801. https://doi.org/10.1175/1520-0493(2001)129<0784:tdcitt>2.0.co;2

Zuluaga, M. D., & Houze, R. A., Jr. (2013). Evolution of the population of precipitating convective systems over the equatorial Indian Ocean in active phases of the Madden–Julian oscillation. *Journal of the Atmospheric Sciences*, *70*(9), 2713–2725. https://doi.org/10.1175/jas-d-12-0311.1